The *NuSTAR* extragalactic survey of the *James Webb Space Telescope* North Ecliptic Pole time-domain field

X. Zhao [1,2]★ F. Civano,[1] F. M. Fornasini [1,3] D. M. Alexander,[4] N. Cappelluti,[5] C. T. Chen [6] S. H. Cohen,[7] M. Elvis,[1] P. Gandhi,[8] N. A. Grogin,[9] R. C. Hickox,[10] R. A. Jansen,[7] A. Koekemoer [9] G. Lanzuisi,[11] W. P. Maksym,[1] A. Masini,[12] D. J. Rosario [4] M. J. Ward,[4] C. N. A. Willmer[13] and R. A. Windhorst[7]

[1]*Center for Astrophysics | Harvard & Smithsonian, 60 Garden Street, Cambridge, MA 02138, USA*
[2]*Department of Physics & Astronomy, Clemson University, Clemson, SC 29634, USA*
[3]*Department of Physics and Astronomy, Stonehill College, 320 Washington Street, Easton, MA 02357, USA*
[4]*Centre for Extragalactic Astronomy, Department of Physics, Durham University, South Road, Durham DH1 3LE, UK*
[5]*Physics Department, University of Miami, Coral Gables, FL 33124, USA*
[6]*Astrophysics Office, NASA Marshall Space Flight Center, ZP12, Huntsville, AL 35812, USA*
[7]*School of Earth and Space Exploration, Arizona State University, P.O. Box 871404, Tempe, AZ 85287, USA*
[8]*Department of Physics and Astronomy, University of Southampton, Highfield, Southampton SO17 1BJ, UK*
[9]*Space Telescope Science Institute, 3700 San Martin Drive, Baltimore, MD 21218, USA*
[10]*Department of Physics and Astronomy, Dartmouth College, 6127 Wilder Laboratory, Hanover, NH 03755, USA*
[11]*INAF, Osservatorio di Astrofisica e Scienza dello Spazio di Bologna, via P. Gobetti 93/3, I-40129 Bologna, Italy*
[12]*SISSA, Via Bonomea 265, I-34151 Trieste, Italy*
[13]*Steward Observatory, University of Arizona, 933 N. Cherry Avenue Tucson, AZ 85721, USA*

ABSTRACT

We present the *NuSTAR* extragalactic survey of the *James Webb Space Telescope* (*JWST*) North Ecliptic Pole (NEP) Time-Domain Field. The survey covers a ~0.16 deg² area with a total exposure of 681 ks acquired in a total of nine observations from three epochs. The survey sensitivities at 20 per cent of the area are 2.39, 1.14, 2.76, 1.52, and 5.20×10^{-14} erg cm^{-2} s^{-1} in the 3–24, 3–8, 8–24, 8–16, and 16–24 keV bands, respectively. The NEP survey is one of the most sensitive extragalactic surveys with *NuSTAR* so far. A total of 33 sources were detected above 95 per cent reliability in at least one of the five bands. We present the number counts, log$N$-log$S$, measured in the hard X-ray 8–24 and 8–16 keV bands, uniquely accessible by *NuSTAR* down to such faint fluxes. We performed source detection on the *XMM–Newton* and *Chandra* observations of the same field to search for soft X-ray counterparts of each *NuSTAR* detection. The soft band positions were used to identify optical and infrared associations. We present the X-ray properties (hardness ratio and luminosity) and optical-to-X-ray properties of the detected sources. The measured fraction of candidate Compton-thick ($N_{\rm H} \geq 10^{24}$ cm^{-2}) active galactic nuclei, derived from the hardness ratio, is between 3 and 27 per cent. As this survey was designed to have variability as its primary focus, we present preliminary results on multiepoch flux variability in the 3–24 keV band.

Key words: surveys – galaxies: active – X-rays: galaxies.

1 INTRODUCTION

Active galactic nuclei (AGN), which represent the rapidly growing phase of supermassive black holes (SMBHs; Soltan 1982; Merloni & Heinz 2008), radiate across the whole electromagnetic spectrum from radio to gamma-ray. X-ray surveys are the most efficient methods to identify and trace the AGN population as accretion processes dominate the emission in the X-ray band. Moreover, X-rays are insensitive to obscuration up to high column density ($N_{\rm H} \sim 10^{23}$ cm^{-2}). Thus, X-ray surveys are able to detect a fairly complete AGN population even with large obscuration and faint luminosities. Indeed, multiple X-rays surveys with *Chandra* and *XMM–Newton*

have been performed in the last 20 yr, covering a wide range of area and flux (Hasinger et al. 2007; Elvis et al. 2009; Civano et al. 2016; Luo et al. 2016; Chen et al. 2018; Siemiginowska & Civano 2019). These works have successfully identified AGN across various redshifts and luminosities, thus measuring the demographics and evolution of both the obscured ($N_{\rm H} \geq 10^{22}$ cm^{-2}) and unobscured ($N_{\rm H} < 10^{22}$ cm^{-2}) AGN population up to $z \approx 5$ (Ueda et al. 2014; Aird et al. 2015; Miyaji et al. 2015; Marchesi et al. 2016b; Vito et al. 2017).

The cosmic X-ray background (CXB), i.e. the diffuse X-ray emission observed between 0.5 and 300 keV, is produced by the integrated emission from AGN. Indeed, soft X-ray surveys have resolved ≥80 per cent of the CXB into individual AGN at 2–10 keV and 80–85 per cent in the 0.5–2 keV energy range (Hickox & Markevitch 2006; Cappelluti et al. 2017). At 20–40 keV, before

★ E-mail: xiurui.zhao@cfa.harvard.edu

the launch of the Nuclear Spectroscopic Telescope Array (*NuSTAR*; Harrison et al. 2013), only 1 per cent was resolved by the coded-mask instruments, such as *INTEGRAL* and *Swift*-BAT (Vasudevan, Mushotzky & Gandhi 2013). *NuSTAR* the first focusing hard X-ray telescope in orbit is 100 times more sensitive than the previous high energy instruments, and thus capable to probe AGN up to high redshift ($z \geq 2$). Indeed, *NuSTAR* has resolved ∼35–60 per cent of the CXB at 8–24 keV (Harrison et al. 2016; Hickox et al. in preparation).

As part of the PI guaranteed time, a series of extragalactic surveys were performed by *NuSTAR* covering from small areas with deep exposures to wide and shallow surveys: the Extended *Chandra* Deep Field–South (ECDFS, 0.33 deg², Mullaney et al. 2015), the Cosmic Evolution Survey field (COSMOS, 1.7 deg²; Civano et al. 2015), and the Serendipitous survey (13 deg²; Lansbury et al. 2017; Klindt et al. in preparation). The strategy was then implemented by a few more surveys: the Ultra Deep Survey (UDS) of the UKIRT Infrared Deep Sky Survey (UKIDSS, 0.6 deg²; Masini et al. 2018a), which further constrained the fraction of Compton-thick (CT-, $N_H \geq 10^{24}$ cm⁻²) AGN in hard X-rays, the Extended Groth Strip survey (EGS, 0.25 deg²; Aird et al. in preparation), and the *Chandra* Deep Field–North survey (CDFN, 0.07 deg²).

During the first call for very large *NuSTAR* proposals (Cycle 5), our team (PI: Civano) was awarded 585 ks to observe with *NuSTAR* a new extragalactic field of interest, the *James Webb Space Telescope* (*JWST*; Gardner et al. 2006) North Ecliptic Pole (NEP) Time-Domain Field (Jansen & Windhorst 2018).

This field was selected by Jansen & Windhorst (2018) to be located within *JWST*'s northern continuous viewing zone (CVZ). *JWST* Interdisciplinary Scientist (IDS) R. Windhorst allocated ∼47 hours of his guaranteed time (programme *JWST*-GTO-1176), to be executed in Cycle 1 after launch and on-orbit validation of *JWST*. The *JWST* NEP Time-Domain Field has become a new and promising field for both time domain studies and population studies, due to its low Galactic foreground extinction, absence of bright foreground stars, and continuous visibility. Indeed, during the past few years, broad community interest has rapidly grown the *JWST* NEP Time-Domain Field into a comprehensive multiwavelength survey. The multiwavelength coverage of *JWST* NEP Time-Domain Field[1] obtained or approved to date includes *JWST*/NIRCam + NIRISS (PI: Windhorst & Hammel), *HST*/WFC3 + ACS (PI: Jansen), *LBT*/LBC (PI: Jansen), *Subaru*/HSC (PI: Hasinger & Hu), *J-PAS* (PI: Bonoli & Dupke), *GTC*/HiPERCAM (PI: Dhillon), *TESS* (PI: Berriman & Holwerda), *MMT*/MMIRS + Binospec (PI: Willmer), *JCMT* (PI: Smail & Im), *IRAM*/NIKA 2 (PI: Cohen), *VLA* (PI: Windhorst & Cotton), *VLBA* (PI: Brisken), *LOFAR* (PI: Van Weeren), *Chandra* (PI: Maksym).

In particular, hard X-ray coverage of infrared (IR) fields, which are known to be unbiased to detecting even the most heavily obscured CT-AGN (see a recent review, Padovani et al. 2017), is important for understanding the properties (e.g. the obscuration) of the IR detected AGN (e.g. Gandhi et al. 2009). The approved 8-band *JWST*/NIRCam imaging and all the photometric and spectroscopic data already available will further constrain the nature of the galaxy hosts, and yield accurate redshifts of hard X-ray-detected sources.

In this paper, we present the 0.16 deg² *NuSTAR* extragalactic survey in the *JWST* NEP Time-Domain Field. The paper is organized as follows. In Section 2, we describe the *NuSTAR* observations and data processing. In Section 3, we describe the simulations and the resulting reliability and completeness of our source detection

Table 1. Details of the individual *NuSTAR* observations.

ObsID	Date	RA (deg)	Dec. (deg)	Exp. (ks)
60511001002	2019-09-30	260.8728	65.8221	73.5
60511002002	2019-10-02	260.7727	65.8220	77.6
60511003002	2019-10-04	260.6360	65.8246	68.7
60511004002	2020-01-03	260.5416	65.9071	89.8
60511005002	2020-01-04	260.7314	65.8736	84.7
60511006002	2020-01-05	260.9080	65.9067	83.0
60511007002	2020-03-01	260.5283	65.7657	65.2
60511008001	2020-03-02	260.7546	65.7483	70.2
60511009001	2020-03-03	260.9508	65.7456	68.3

technique. In Section 4, we present the X-ray properties of the sources detected in the *NuSTAR* NEP survey. In Section 5, we present the soft X-ray, optical, and IR counterparts of the *NuSTAR*-detected sources and their properties. In Section 6, we discuss the CT fraction and X-ray variability of the sources detected in the *NuSTAR* NEP survey. In the Appendix, we present the point source catalogue. Uncertainties are quoted at 90 per cent confidence level throughout the paper unless otherwise stated. Standard cosmological parameters are adopted as follows: $\langle H_0 \rangle = 70$ km s⁻¹ Mpc⁻¹, $\langle \Omega_M \rangle = 0.3$, and $\langle \Omega_\Lambda \rangle = 0.7$.

2 DATA PROCESSING

The *NuSTAR* survey of the *JWST* NEP Time-Domain Field consists of nine observations with a total exposure time of ∼681 ks acquired during the *NuSTAR* GO cycle 5 (PI: Civano). The survey was designed to have variability as its primary focus, therefore the field was observed in three epochs during 2019 October, 2020 January, and 2020 March. Details about each observation are listed in Table 1.

2.1 Data reduction

The *NuSTAR* data were reduced using HEASoft v.6.27.2 and *NuS-TAR* Data Analysis Software (NuSTARDAS) v.1.9.2 with CALDB v.20200526. The level 1 raw data were calibrated, cleaned, and screened by running the nupipeline script.

Following Civano et al. (2015, hereafter C15), we produced the full-field light curves in the low energy band (3.5–9.5 keV) with a bin size of 200 s using xselect to search for high-background time intervals. We screened all nine observations and cleaned the intervals with count rates that were more than a factor of ∼2 higher than the average count rate in that observation. The resulting loss of exposure time corresponds to 0.4–2.6 per cent of the individual exposure times of the nine observations. The total exposure loss of the two *NuSTAR* focal plane modules are 9.3 ks for FPMA and 7.0 ks for FPMB, which is ∼1.2 per cent of the total *NuSTAR* NEP survey exposure time. We then re-ran nupipeline applying the good time intervals (GTI) after cleaning the high-background time intervals. Due to the strong instrumental emission lines between 25 and 35 keV, we imposed a high energy cut at 24 keV in our analysis, which is the standard limit adopted in previous *NuSTAR* survey studies. Therefore, we filtered the data products of this work into six energy bands (3–24, 3–8, 8–24, 8–16, 16–24, and 35–55 keV).

2.2 Exposure map production

The exposure maps were generated in four energy bands 3–24, 3–8, 8–24, and 35–55 keV using the NuSTARDAS tool nuexpomap, which computes the effective exposure time for each pixel on the

[1]http://lambda.la.asu.edu/jwst/neptdf/
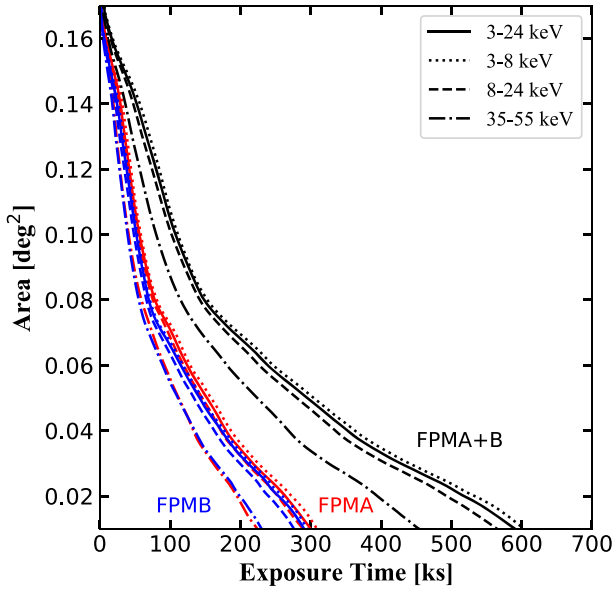
Figure 1. Cumulative survey area as a function of the effective vignetting-corrected exposure time for FPMA (red), FPMB (blue), and the summed FPMA + B (black) in four energy bands: 3–24 keV (solid line), 3–8 keV (dotted line), 8–24 keV (short dashed line), and 35–55 keV (dash–dotted line).

detectors. We adopted the 8–24 keV exposure map as the exposure maps of 8–16 keV and 16–24 keV energy bands due to the marginal differences between their exposure maps. By using the 8–24 keV exposure map, the 8–16 keV exposure is underestimated by at most 3 per cent and the 16–24 keV exposure is overestimated by at most 12 per cent (Masini et al. 2018a). The created exposure maps account for detector bad and hot pixels, detector gaps, attitude variations, mast movements, and telescope vignetting. Since vignetting is heavily energy-dependent, the exposure map of each desired energy band was weighted assuming a power-law spectrum with photon index $\Gamma = 1.80$. The mean, spectrally weighted energies are 9.88 keV for 3–24 keV band, 5.42 keV for 3–8 keV band, 13.02 keV for 8–24 keV band, and 44.35 keV for 35–55 keV. The exposure maps were produced, using a bin size of 5 pixels (12.3 arcsec) to reduce the calculation time. The exposure map binning is significantly smaller than the *NuSTAR* point spread function (PSF; half power diameter ≈ 60 arcsec) and is smaller than the aperture size that we use to perform photometry analysis. The vignetting corrected exposure maps for each observation were then merged into a mosaic for each energy band using the HEASoft tool `ximage`. The cumulative area as a function of the effective exposure time for each energy band and for different focal plane modules (FPMA, FPMB, and the summed FPMA + B) is plotted in Fig. 1. A small difference of < 8 per cent in the effective exposure time is seen between FPMA and FPMB, with FPMA being more sensitive, which is consistent with the expectations.

2.3 Mosaic creation

We merged the nine observations into three mosaics (FPMA, FPMB, and the summed FPMA + B) using the HEASoft tool `ximage`. The mosaics are filtered into six energy bands 3–24, 3–8, 8–24, 8–16, 16–24, and 35–55 keV, using the `xselect` tool. We did not perform any astrometric offset correction to our data since only one bright object is observed in the *NuSTAR* NEP field, which prevents

us from testing the significance of the astrometric offset as has been done in the previous surveys. C15 found a 1–7 arcsec astrometric offset in the *NuSTAR* COSMOS survey using a stacking technique. Therefore, we assume that the astrometric offset only marginally affects the sensitivity of our final mosaic images. The mosaics in the 3–24 and 3–8 keV bands are presented in Fig. 2. To achieve the deepest sensitivity, we performed source detections and simulations using the summed FPMA + B mosaic in each energy band.

2.4 Background map production

The *NuSTAR* background includes four independent components that vary spatially across the detectors and the two telescopes. Here, we briefly introduce the different background components (refer to Wik et al. 2014 for more details). Below ~ 20 keV, the background is dominated by stray light from the unblocked sky through the aperture stops of *NuSTAR*, which is spatially non-uniform across the field of view (FoV). Below ~ 10 keV, the X-rays from the CXB which are focused by the optics (fCXB), also contribute to the *NuSTAR* background. The fCXB component is spatially non-uniform among the four detectors. The solar photons reflected by the back of the aperture stop can also contribute to the background at low energy (< 5 keV). This solar component is time variable depending on whether or not the instrument is in sunlight. Since the NEP survey was conducted during the solar minimum, our observations were not significantly affected by this solar component. Above 20 keV, the background is dominated by instrumental emission lines produced by interactions between the detectors and radiation in-orbit. We analysed the background of each *NuSTAR* observation using `nuskybgd`[2] (Wik et al. 2014), which includes all the aforementioned components. We followed the same procedure as in C15 to produce the background of each observation for both FPMA and FPMB. To ensure the accuracy of the generated background maps, we extract and compare the number of counts of the observations and their corresponding simulated maps. We evenly divided the FoV into 64 circular (45 arcsec in radius) subregions. The mean difference between the number of counts are (Data – Bgd)/Bgd $= -0.7$ per cent and 2.3 per cent for FPMA and FPMB, respectively. The standard deviations of the per cent differences are 12.6 per cent and 14.2 per cent for FPMA and FPMB, respectively. The normalized distribution of (Data – Bgd)/Bgd of FPMA and FPMB are plotted in Fig. 3, which shows a good agreement between the generated background maps and the observed data.

3 SIMULATIONS

To test and optimize our source detection method, following C15, we perform an extensive set of simulations (1200 for each energy band[3]). Comprehensive simulations are essential to determine the reliability and completeness of the source list and to measure the positional accuracy of the detections.

3.1 Generating simulated data

To produce the simulated maps, we used the same strategy as in C15. We generated a sample of mock sources with fluxes assigned

[2]https://github.com/NuSTAR/nuskybgd
[3]To build enough statistics, we performed a larger number of simulations than C15 (300 for each energy band) as the area covered by *NuSTAR* NEP is 14 times smaller than *NuSTAR* COSMOS.
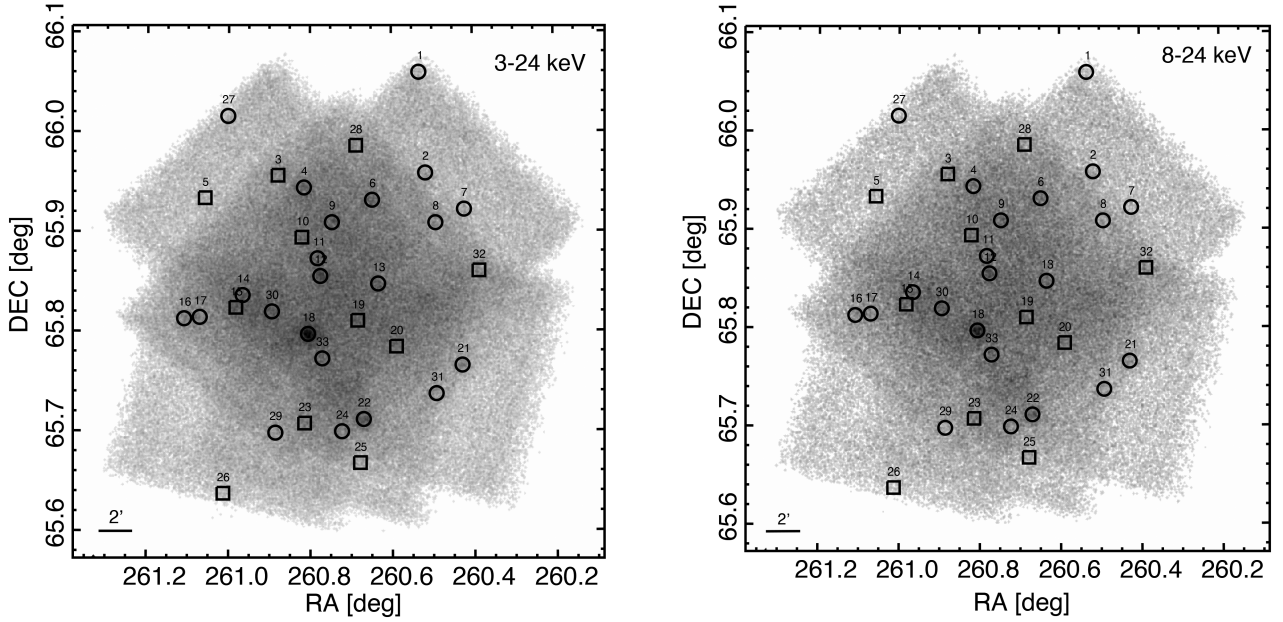
Figure 2. *NuSTAR* FPMA + FPMB 3–24 keV (left) and 8–24 keV (right) mosaics. The positions of the *NuSTAR* detected sources with (black circle, 25 arcsec radius) and without (black square, 45 arcsec width) soft X-ray counterparts are plotted.
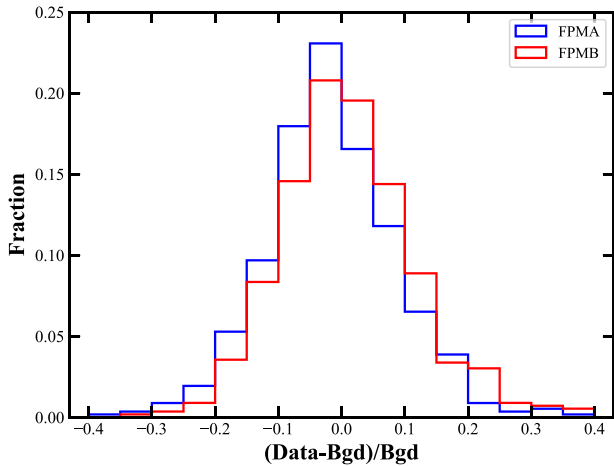
Figure 3. Normalized distributions of relative differences between counts extracted from observed data and background maps in each observation for FPMA (red) and FPMB (blue).

randomly from the log$N$–log$S$ distribution measured in Treister, Urry & Virani (2009). The minimum flux for the input sources is set to be 3×10^{-15} erg cm^{-2} s^{-1} in the 3–24 keV band (about 10 times fainter than the expected flux limit of the survey) to ensure the completeness of the simulation. Fluxes in the 3–8, 8–16, 8–24, and 16–24 keV bands are extrapolated from the 3–24 keV flux, using an absorbed power-law spectral model with $\Gamma = 1.80$ and a Galactic absorption of $N_H = 3.4 \times 10^{20}$ cm^{-2} (HI4PI Collaboration et al. 2016). The fluxes of the simulated sources were converted to count rates using count-rate-to-flux conversion factors (CF) of 4.86, 3.39, 7.08, 5.17, and 16.2 $\times 10^{-11}$ erg cm^{-2} counts^{-1} in the 3–24, 3–8, 8–24, 8–16, and 16–24 keV bands, respectively. The CF were computed using WebPIMMS,[4] assuming the above spectral model.

The simulated maps were created by randomly placing the generated mock sources on the background mosaic produced in Section 2.4 but without an fCXB component (since the fCXB is made up of the emission from the undetected discrete sources). Mock source counts were computed using their count rates and the effective exposure at the source location. The counts associated with each mock source were spatially distributed on the background map according to the PSF. The emission from mock sources accounts for only a fraction of the fCXB component. Thus, to match the total number of counts in the observed NuSTAR mosaic, we randomly distributed additional background counts (<9 per cent of the total) on the simulated maps, which were drawn from the background map including only the fCXB component. The fCXB normalization was averaged across all the fields, and re-scaled to account for the 'missing' counts associated with the unresolved fCXB. These additional counts are due to the fact that the unresolved sources fainter than 3×10^{-15} erg cm^{-2} s^{-1} were not included in the simulations. A Poisson realization of the simulated map (mock sources plus background) was generated. With the above procedure, we generated a set of 1200 simulated maps in five energy bands (3–24, 3–8, 8–24, 8–16, and 16–24 keV) for both FPMA and FPMB, which were then combined to create the FPMA + B simulated maps. The position, exposure time, and flux of each mock source were recorded in an input source catalogue for each simulation.

3.2 Source detection on simulated maps

Once we made the simulated maps with mock sources, we performed source detection on the simulated maps, following the technique developed in Mullaney et al. (2015). We performed the source detection on the false-probability maps, which measure the possibility that a signal is due to a background fluctuation rather than from a real source. The false-probability maps were generated with the smoothed simulated maps and the background mosaics using the incomplete Gamma function. The false probability at each pixel on the map was calculated using the igamma function in

Table 2. Mean number of the detected sources using SExtractor in the simulated maps (line 1). Mean number of the detected sources matched to the input source catalogue within 30 arcsec (line 2). The DET ML threshold at 99 per cent reliability (line 3–5) and at 95 per cent reliability (line 6–8) for each exposure intervals. Mean number of the detected sources with DET ML above 99 per cent and 95 per cent reliability threshold in the simulated maps (line 9,10) and in the real data (line 11,12).

	3–24 keV	3–8 keV	8–24 keV	8–16 keV	16–24 keV
Detections in simulated maps	393	186	191	184	180
Matched to Input	50	46	37	37	21
DET ML(99 per cent, 20–200 ks) threshold	13.53	13.95	15.48	14.43	16.35
DET ML(99 per cent, 200–500 ks) threshold	12.00	12.18	13.75	13.10	15.94
DET ML(99 per cent, >500 ks) threshold	10.99	11.02	13.13	12.30	15.72
DET ML(95 per cent, 20–200 ks) threshold	11.47	11.65	12.99	12.35	15.35
DET ML(95 per cent, 200–500 ks) threshold	9.89	10.10	11.54	10.88	14.42
DET ML(95 per cent, >500 ks) threshold	8.89	8.89	10.67	10.22	14.05
Simulated maps					
DET ML > 99 per cent reliability threshold	14.4	11.4	4.8	5.6	0.5
DET ML > 95 per cent reliability threshold	21.1	17.0	7.4	8.5	0.6
Real data					
DET ML > 99 per cent reliability threshold	16	15	4	10	1
DET ML > 95 per cent reliability threshold	26	19	8	11	1

IDL, i.e. $P_{\text{false}} = \text{igamma}(C_{\text{data}}, C_{\text{bgd}})$, where C_{data} is the number of counts of the simulated data in that pixel and C_{bgd} is the number of counts of the corresponding background mosaics in that pixel:

$$P_{\text{false}} = \frac{\int_0^{C_{\text{bgd}}} e^{-x} x^{C_{\text{data}}-1} \mathrm{d}x}{\int_0^{\infty} e^{-x} x^{C_{\text{data}}-1} \mathrm{d}x}. \tag{1}$$

Before creating the false-probability maps, we smoothed the simulated maps and the background mosaics using circular top-hat functions with 20 arcsec radius to ensure the detection of faint sources. We used SExtractor (Bertin & Arnouts 1996) to detect the sources on the obtained smoothed false-probability maps in each energy band. The false-probability was converted to $-\log(P_{\text{false}})$ as the input to SExtractor. The detection limit was set to $P_{\text{false}} \leq 10^{-2.5}$ ($\sim 3\sigma$) to make sure that we detected all potentially faint sources. The local minimum P_{false} positions are recorded as the coordinate of each detection. We then define the maximum likelihood (DET ML) for each detection using the inverse of the logarithm of the Poisson probability that a detection is due to a random fluctuation of the background (P_{random}), i.e. DET ML $= -\ln P_{\text{random}}$. The Poisson probability is calculated using the total and background counts extracted from the simulated map and the corresponding background map at the coordinate of the detection using a circular aperture of 20 arcsec radius. A lower DET ML suggests a higher chance that the signal is from the background fluctuation at that position.

After performing the source detection, we obtain a catalogue of detections for each simulation and each energy band. The average numbers of sources detected above the detection limit in each band are listed in Table 2. The counts associated with each detected source may be contaminated by the nearby sources within 90 arcsec due to the point spread function. Therefore, we apply a deblending process to the detections in the catalogues of each simulation following the technique in Mullaney et al. (2015). The deblended source counts and background counts were then used to compute updated DET ML values for each detection. The detections were matched with the input catalogue, using a 30 arcsec separation limit. The average numbers of matched sources for each simulation in five energy bands are reported in Table 2.

3.3 Reliability, completeness, positional uncertainty

With extensive simulations, we calculate the reliability and completeness of our source detection technique. Reliability is the ratio of the number of the detected sources matched to input sources to the total number of detected sources at or above a particular DET ML. For example, if 100 sources were detected above a certain DET ML and 95 of them had counterparts from the input source catalogue, then the reliability of the source detection at that DET ML is 95 per cent. Completeness is defined as the ratio of the number of the detected sources that are matched to the input catalogue and are above a chosen reliability threshold to the number of the sources in the input catalogue at a particular flux. For example, if 50 sources were detected and with DET ML are above 95 per cent reliability threshold at a particular flux, then the completeness at that flux is 50 per cent at 95 per cent reliability level if there are 100 input sources at that flux. Sources with larger DET ML are considered to be more reliable, but a higher DET ML threshold leads to lower completeness. Therefore, to determine the detection criteria for the actual observations, we need to maximize both the survey completeness and reliability.

We found that the ratio of the spuriously detected sources to all detected sources decreases exponentially as the exposure time increases. Thus, the reliability curve as a function of DET ML is exposure-dependent as well. Due to the design of the *NuSTAR* NEP survey, the exposure time across the field is non-uniform. We analyse the reliability function at three different exposure intervals (combined FPMA + FPMB), i.e. 20–200 ks, 200–500 ks, and >500 ks. We applied an exposure cut-off at 20 ks to avoid potentially spurious detections on the edge of the observations. The 200 and 500 ks values were chosen to evenly separate the total exposure ~680 ks (see Fig. 1). In the left-hand panel of Fig. 4, we plot the reliability distribution as a function of DET ML in different exposure intervals. The maximum likelihoods corresponding to 99 and 95 per cent reliability (i.e. 1 and 5 per cent spurious detections) in different exposure intervals are reported in Table 2, respectively. We found that the DET ML thresholds are significantly different among the five energy bands and among different exposure intervals, which was also found in previous studies (e.g. Civano et al. 2015; Masini et al. 2018a). The DET ML thresholds of 3–24 and 3–8 keV are much lower than the DET ML thresholds in hard energy bands, and the DET ML thresholds
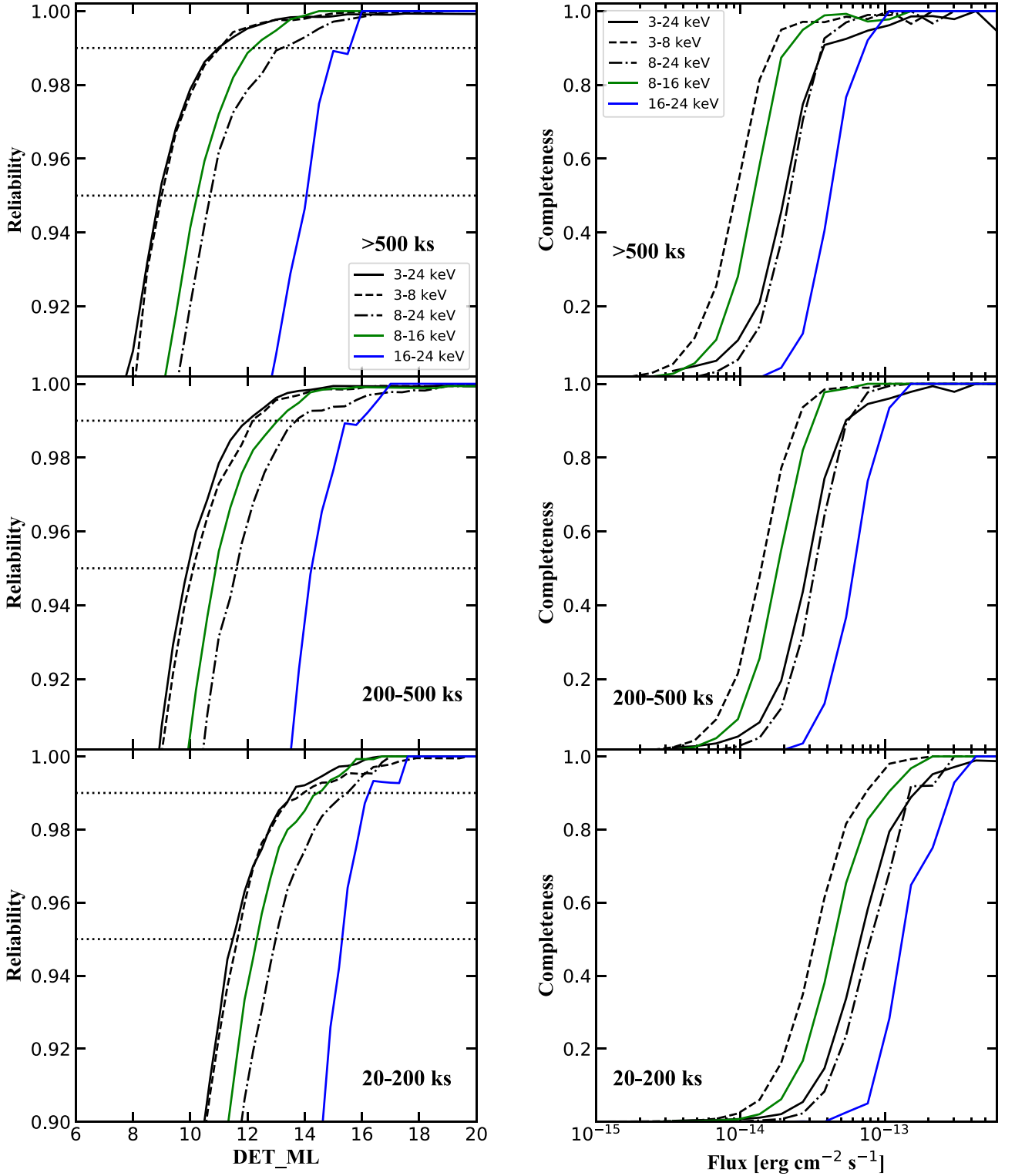
Figure 4. From top to bottom are cumulative reliability as a function of DET ML (left) and completeness as a function of flux (right) in >500 ks (top), 200–500 ks (middle), and 20–200 ks (bottom) exposure intervals. Solid black: 3–24 keV. Dashed black: 3–8 keV. Dash–dotted black: 8–24 keV. Sold green: 8–16 keV. Solid blue: 16–24 keV. The 99 per cent and 95 per cent reliability lines are plotted using dotted black lines on left.

decreases significantly as the exposure time increases. The average numbers of the sources which were detected above 99 and 95 per cent reliability threshold in the simulated maps are reported in Table 2.

After determining the DET ML thresholds for different reliability levels, in the right-hand panel of Fig. 4, we plot the detection completeness as a function of source flux of five energy bands at 95 per cent reliability level in different exposure intervals. The
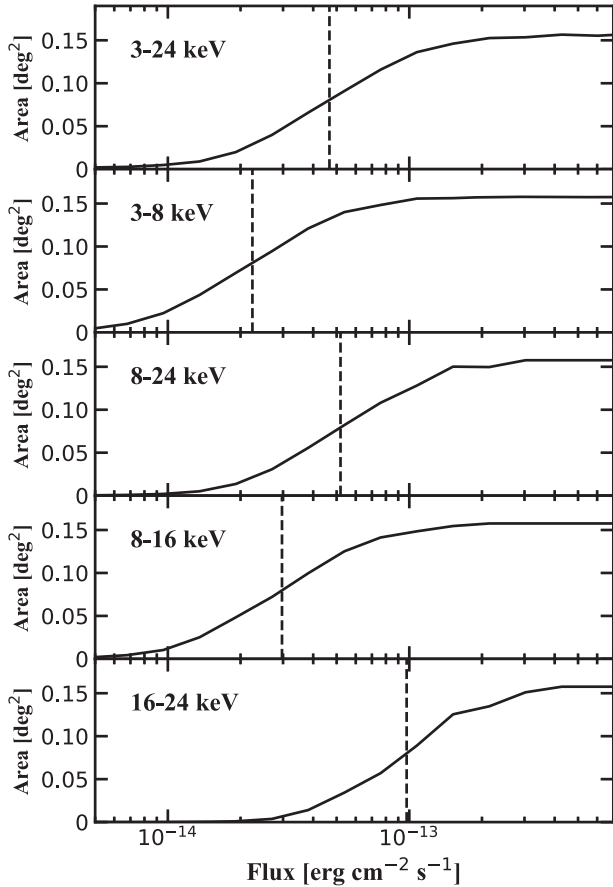
Figure 5. Sky coverage in five energy bands at 95 per cent reliability level. The half-area flux is labelled for each energy band.

completeness curves for each energy band also depend on the exposure intervals, as the completeness value at a certain flux increases significantly as the exposure increases. The completeness is the fraction of the sources in the survey FoV that are detected and above the reliability threshold. Therefore, the completeness corresponds to the normalization of the effective sky-coverage of the survey which is the area covered at a given flux. The sky-coverage of the survey at a particular flux is thus the completeness of the survey at that particular flux multiplied by the maximum covered area exhibited in the exposure map. The total sky-coverage of the survey was calculated by adding up the sky-coverage curves of all three exposure intervals. The half-area fluxes are 4.67, 2.24, 5.19, 2.97, and 9.75×10^{-14} erg cm^{-2} s^{-1} for 3–24, 3–8, 8–24, 8–16, and 16–24 keV, respectively. The fluxes at 20 per cent of the sky-coverage are 2.39, 1.14, 2.76, 1.52, and 5.20×10^{-14} erg cm^{-2} s^{-1} in the 3–24, 3–8, 8–24, 8–16, and 16–24 keV bands, respectively. The sky-coverage of the survey in the five energy bands is plotted in Fig. 5. The hard band (8–24 keV) sky-coverage is plotted in Fig. 6, which is compared with the previous *NuSTAR* surveys (COSMOS; Civano et al. 2015), (ECDFS; Mullaney et al. 2015), (EGS; Aird et al. in preparation), and (Serendipitous; Lansbury et al. 2017). Reaching the deepest flux in the hard X-ray band makes NEP one of the most sensitive *NuSTAR* contiguous surveys to date.

In order to quantify the positional uncertainties of our detections, we plot the distribution of the separation between positions of the input and output detected sources in the 3–24 keV band in Fig. 7 using solid lines. The separation distribution follows a Rayleigh
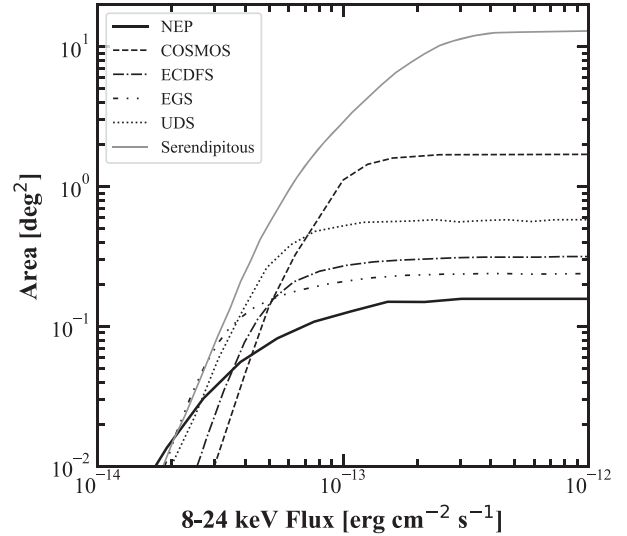

Figure 6. Hard band (8–24 keV) sky-coverage of *NuSTAR* surveys: NEP in black solid line, COSMOS (Civano et al. 2015) in dashed line, ECDFS (Mullaney et al. 2015) in dash–dotted line, EGS (Aird et al. in preparation) in dash–dot–dotted line, UDS (Masini et al. 2018a) in dotted line, and Serendipitous survey (Lansbury et al. 2017) in grey solid line.
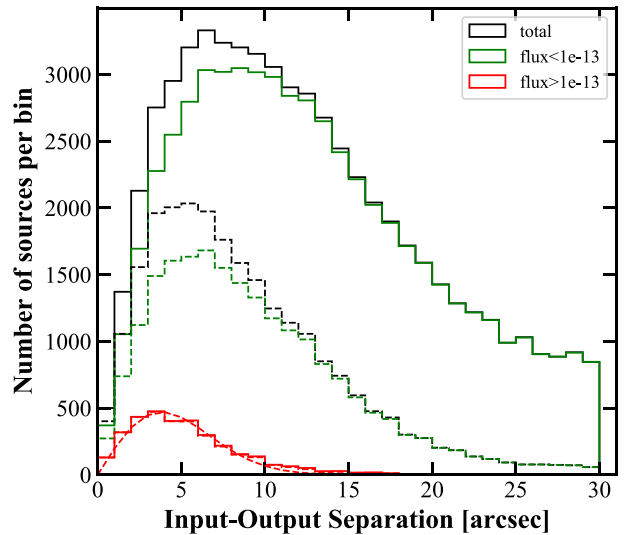
Figure 7. Distributions of input to detected positions in the 3–24 keV bands for the 1200 simulations. Solid refer to the whole sample and dashed lines refer only to sources above the 95 per cent reliability DET ML thresholds. The black lines represent the distribution of total sources, the green lines represent the distribution for sources with 3–24 keV flux $<10^{-13}$ erg cm^{-2}s^{-1}, and the red lines represent sources with brighter fluxes. The dashed red curve is the best Rayleigh fit of the input–output separation of the bright sources above the 95 per cent reliability DET ML threshold.

distribution (Pineau et al. 2017), thus we performed a Rayleigh fitting of the detected separation distribution. We found a best-fitting Rayleigh scale parameter of $\sigma_{\text{all}} = 9.7$ arcsec for all matched sources. The separations between the input and output detected positions are significantly improved when only using the sources with DET ML above 95 per cent reliability threshold ($\sigma_{95\,\text{per cent}} = 6.3$ arcsec). The input–output separations are smaller for brighter sources with 3–24 keV flux $>10^{-13}$ erg cm^{-2}s^{-1} ($\sigma_{95\,\text{per cent,bright}} = 3.8$ arcsec) than the fainter sources ($\sigma_{95\,\text{per cent,faint}} = 6.9$ arcsec). The fitted separations
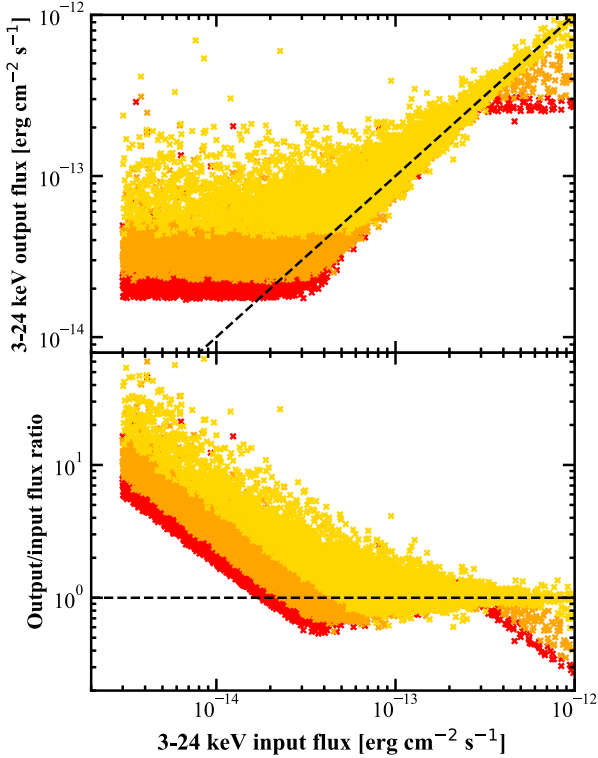
Figure 8. Upper: 3–24 keV input fluxes versus the measured fluxes of the sources with DET ML above the 95 per cent reliability threshold in the simulations with exposure of >500 ks (red), 200–500 ks (orange), and 20–200 ks (yellow). Lower: Ratio between measured fluxes and input fluxes as a function of input fluxes.

are consistent with previous work. Therefore, we can adopt their distribution as the expected positional uncertainty of true detections.

3.4 Fluxes

The flux of each matched source in the simulations was computed in different energy bands. We extracted the source counts and deblended background counts of each matched source using the CIAO (Fruscione et al. 2006) tool `dmextract`. The net counts were then converted to fluxes using the exposure time at the source position and the count-rate-to-flux CF mentioned in Section 3. Since the counts were extracted in a 20 arcsec area, we convert this aperture flux to the total flux using a factor, i.e. $F_{20''}/F_{\rm tot} = 0.32$, calculated from the *NuSTAR* PSF.[5] We used a single $F_{20''}/F_{\rm tot}$ for FPMA and FPMB and for different energy bands as we found them to be consistent. In Fig. 8, we plot the 3–24 keV input fluxes ($F_{\rm in}$) and the measured 3–24 keV fluxes of the corresponding matched sources with DET ML above 95 per cent reliability threshold in different exposure intervals. The flux limits of the detections are $\sim 1.7 \times 10^{-14}\,{\rm erg\,cm^{-2}\,s^{-1}}$ for >500 ks exposure interval, $\sim 2.2 \times 10^{-14}\,{\rm erg\,cm^{-2}\,s^{-1}}$ for 200–500 ks exposure interval, and $\sim 4.2 \times 10^{-14}\,{\rm erg\,cm^{-2}\,s^{-1}}$ for 20–200 ks exposure interval, which are consistent with the flux limits of the completeness curves shown in the right panel of Fig. 4. As seen in Fig. 8, at faint fluxes ($F_{\rm in} < 5 \times 10^{-14}\,{\rm erg\,cm^{-2}\,s^{-1}}$) that approach the detection limit, the measured flux distribution widens due to

---

Table 3. Distribution of the detected sources in the 95 per cent reliability catalogue. F(f), S(s), and H(h) represent 3–24, 3–8, 8–24 keV (and/or 8–16 and 16–24 keV). F, S, H represent sources detected and above the 95 per cent reliability threshold in the given energy band, while f, s, and h refer to the sources detected but below the 95 per cent reliability threshold.

|	
F + S + H	9 (27 per cent)
F + S + h	6 (18 per cent)
F + S	1 (3 per cent)
F + s + h	5 (15 per cent)
F + s	3 (9 per cent)
F + h	2 (6 per cent)
f + S + h	1 (3 per cent)
f + S	1 (3 per cent)
S	1 (3 per cent)
f + s + H	1 (3 per cent)
f + H	2 (6 per cent)
H	1 (3 per cent)

the Eddington bias. At bright fluxes ($F_{\rm in} > 3 \times 10^{-13}\,{\rm erg\,cm^{-2}\,s^{-1}}$), the measured values might be underestimated due to the fixed aperture used to extract the *NuSTAR* counts. This underestimated effect does not impact the flux measurement of the bright sources in the NEP survey, since the 3–24 keV flux of the brightest source is $2.8 \times 10^{-13}\,{\rm erg\,cm^{-2}\,s^{-1}}$ (see Section 4).

4 SOURCE CATALOGUE

We performed source detection on the observed data using the same technique as described in Section 3.2 by using SExtractor. We extracted the total counts and the deblended background counts of the detected sources on the FPMA + FPMB mosaics and the simulated background maps using a 20 arcsec radius aperture. Using the extracted counts, we calculated DET ML of each detection in different energy bands. Thus, we generated a catalogue of sources having DET ML above the 99 per cent and 95 per cent reliability thresholds for each energy band. Then we merged the catalogue of each band to make a master catalogue by performing a positional matching (30 arcsec in radius) among the catalogues of five energy bands. The master catalogue consists of the sources that are detected and pass the DET ML thresholds in at least one energy band (including both matched and unmatched sources). It is worth noting that the DET ML thresholds depend on the source exposure. The master catalogue contains 21 sources above the 99 per cent reliability threshold and 33 sources above the 95 per cent reliability threshold. In the following discussion, we focus on the 95 per cent reliability catalogue. Statistically, we expected ∼2 spurious detections in the 95 per cent reliability catalogue (summing the expected number of spuriously detected sources in each band). We report the distribution of the detected sources in the master catalogue in Table 3, including sources that are detected and pass above the 95 per cent reliability threshold labeled with capital F, S, and H for 3–24, 3–8, and 8–24 keV (and/or 8–16 keV and 16–24 keV), and sources that are detected but fall below the threshold labeled with lower case f, s, and h in given energy bands.

The coordinates of the sources listed in the final catalogue are taken from the energy band corresponding to the highest DET ML. The position of each detected source is plotted in Fig. 2. The vignetting-corrected exposure times at the positions of the sources are measured in each energy band. The total counts and background counts (deblended if detected and passing the DET ML threshold) of each source in a given energy band are measured at the positions of the sources in a 20 arcsec radius aperture. The net counts (total counts
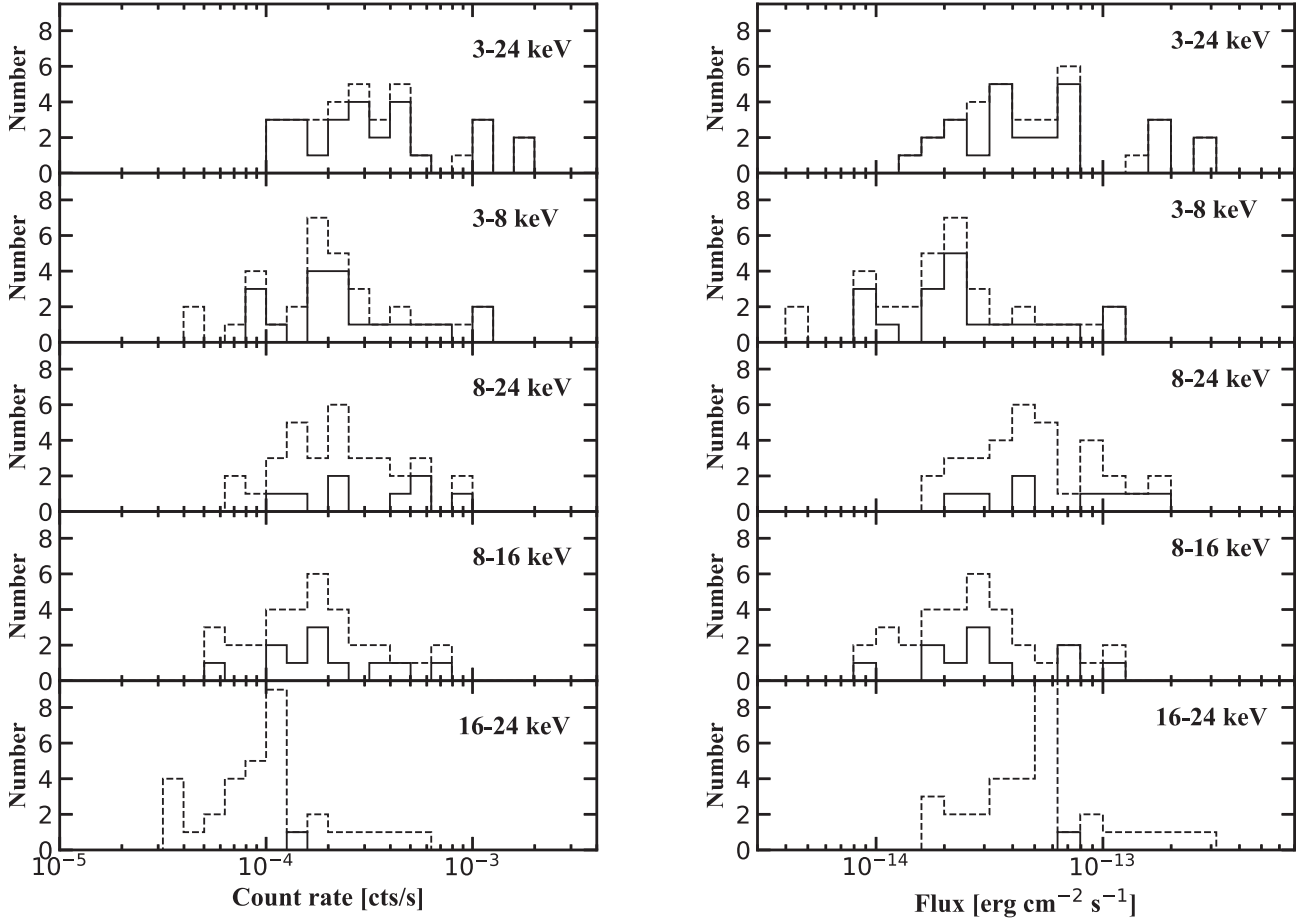
Figure 9. 20 arcsec radius aperture count rate (left) and total flux (right) distributions for sources detected and above threshold (solid line) in the 3–24, 3–8, 8–24, 8–16, and 16–24 keV bands from top to bottom. Upper limits are plotted in dashed lines.

– deblended background counts) and 1σ net counts errors were calculated for the sources that were detected and passed the DET ML threshold in a given energy band. The 90 per cent confidence upper limit of the net counts was calculated for undetected sources, or the sources that were detected but fell below the DET ML threshold in a given energy band. The net counts errors and upper limits were determined using equations (9) and (12) in Gehrels (1986) with $S = 1$ for 1σ confidence level and $S = 1.645$ for 90 per cent confidence level. The count rates are calculated by dividing the net counts by the vignetting-corrected exposure time in a given energy band. The total fluxes in a given energy band were converted from the count rates using the count-rate-to-flux CF described in Section 3 and were corrected the aperture correction factor ($F_{tot}/F_{20''} \sim 0.32$ for 20 arcsec aperture). In Fig. 9, the distribution of the 20 arcsec radius aperture count rates and total fluxes in different energy bands of all sources in the catalogue are plotted (90 per cent confidence upper limits are also included).

We also performed source detection on the data in 35–55 keV band, where the background can be well characterized using `nuskybgd`. By using the same source detection and deblending technique, we computed the DET ML for each detection in SEXTRACTOR. We adopted the DET ML threshold of the 35–55 keV band computed in Masini et al. (2018a), which used the same simulation analysis as we did for other energy bands. We did not find any significant detection that was above the 95 per cent reliability threshold (DET ML = 22.2). The most significant detection in 35–55 keV

band is DET ML = 10.75. The non-detection in 35–55 keV band is consistent with Masini et al. (2018a), who did not detect any source in 35–55 keV band in the $\sim$0.6 deg^2 UDS field.

4.1 log*N*-log*S*

We computed the cumulative log*N*-log*S* distribution in three energy bands (3–8, 8–24, and 8–16 keV), using the sky coverage as a function of flux following Cappelluti et al. (2009). The distribution is defined as

$$N(> S) = \sum_{i=1}^{N_S} \frac{1}{\Omega_i} \text{deg}^{-2}, \tag{2}$$

where $N(> S)$ is the total number of sources detected and passing the 95 per cent reliability threshold in that energy band with flux greater than S. Ω_i is the sky coverage associated with the flux of the ith source. The variance of the number counts is thus defined as

$$\sigma_S^2 = \sum_{i=1}^{N_S} (\frac{1}{\Omega_i})^2. \tag{3}$$

For the minimum flux, we use as a factor of 3 lower than the flux corresponding to 50 per cent of the survey sky-coverage in each band. The maximum flux is 10^{-13} erg cm^{-2} s^{-1} for the 3–8 keV and 8–24 keV bands, and 6×10^{-14} erg cm^{-2} s^{-1} for the 8–16 keV band. The cumulative log*N*–log*S* in the 3–8, 8–24, and 8–16 keV bands
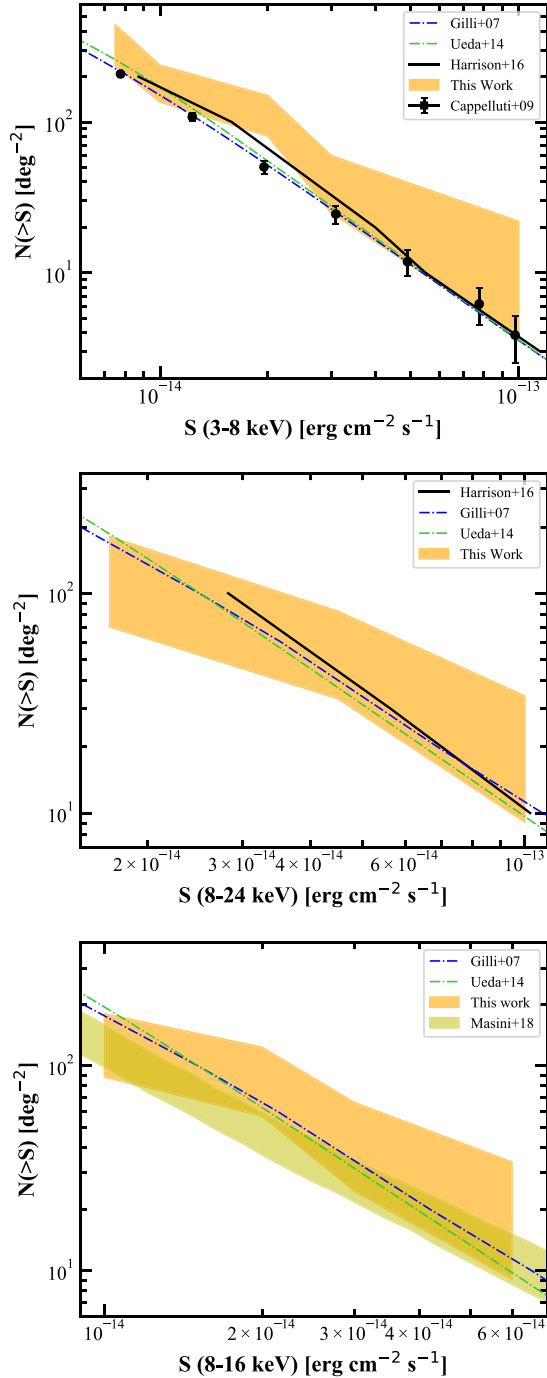
Figure 10. Integral number counts for the 3–8 keV (top), 8–24 keV (middle), and 8–16 keV (bottom) bands. The orange shaded region represents the 68 per cent confidence region on the integrated number counts. The results of our work are compared with those derived in Harrison et al. (2016, black solid line) and Masini et al. (2018b, yellow shaded region) using *NuSTAR*, those derived in Cappelluti et al. (2009) (black points) using *XMM–Newton*, and those constrained by the population synthesis model of CXB (blue dashdot line, Gilli et al. 2007) and (green dash–dotted line, Ueda et al. 2014).

are plotted in Fig. 10. Our work extends the 8–24 keV number counts to lower fluxes than previous work presented in Harrison et al. (2016). The soft band number counts are compared with those derived using *XMM–Newton* by Cappelluti et al. (2009). The 2–10 keV fluxes reported in Cappelluti et al. (2009) are converted to

3–8 keV, assuming a power-law model with photon index $\Gamma = 1.80$. The log$N$–log$S$ constrained by the CXB population synthesis models, e.g. Gilli, Comastri & Hasinger (2007) and Ueda et al. (2014), are shown as points of comparison as well. The 3–8 keV number counts in our work surpass those measured or constrained in the previous observations and models, but are still within the 1σ uncertainties. Our cumulative log$N$-log$S$ in hard energy bands, i.e. 8–24 and 8–16 keV, are in good agreement with the previous results derived from *NuSTAR* (Harrison et al. 2016; Masini et al. 2018b) and with the CXB population synthesis models.

5 MULTIWAVELENGTH COUNTERPARTS

5.1 Soft X-ray counterparts

In order to associate the *NuSTAR* detected sources with the multi-wavelength counterparts, accurate coordinates are needed. The best strategy is first to identify the soft X-ray counterpart of the *NuSTAR*-detected sources, which typically have more accurately measured positions. Currently, there is no public soft X-ray (e.g. *Chandra* and *XMM–Newton*) catalogue in the *JWST* NEP Time-Domain Field.

5.1.1 XMM–Newton

In *NuSTAR* cycle 6, we were granted additional *NuSTAR* observations together with 40 ks *XMM–Newton* observations (PI: Civano) to study hard X-ray variability with simultaneous broad X-ray coverage in the 0.5–24 keV band in the NEP field. The first 10 ks *XMM–Newton* observation was taken on 2020 October 14. The *XMM–Newton* observation covered about 90 per cent of the *NuSTAR* NEP field with the exception of the two bottom corners of the field (where only one *NuSTAR* source, ID 26, was detected).

In order to obtain a list of soft X-ray sources in the *NuSTAR* NEP field, we performed source detection on the first 10 ks *XMM–Newton* observation. We used similar source detection techniques as in the previous *XMM–Newton* surveys (e.g. Brunner et al. 2008; Cappelluti et al. 2009; LaMassa et al. 2016), which are briefly summarized here. The observational data files (ODF) of MOS1, MOS2, and pn were generated using the SAS (version 19.0.0) tasks `emproc` and `epproc`. The background flares of the three instruments were screened using the standard method. Since the *XMM–Newton* background was contaminated by the Al k α fluorescent emission at 1.48 keV in both MOS and pn data and by two Cu lines at $\sim$7.4 and 8.0 keV in pn data, the events between 1.45 and 1.54 keV were removed in both MOS and pn data, and the events in 7.2–7.6 and 7.8–8.2 keV were also removed from the pn data.

The images of the clean event files of MOS1, MOS2, and pn were then generated in the 0.5–2 and 2–10 keV energy bands. To fully utilize the sensitivity of the *XMM–Newton* data, we created the MOS + pn mosaics in each energy band using the SAS `emosaic` task. The exposure maps were generated using the SAS task `eexpmap` for each instrument in the two energy bands. The energy conversion factors (ECFs), used to convert from count rates to flux, were calculated using WebPIMMS for each energy band and each instrument, assuming an absorbed power-law model with $\Gamma = 1.80$ and Galactic column density of $N_H = 3.4 \times 10^{20}$ cm^{-2}. The ECFs for MOS and pn are 0.54 and 0.15 $\times 10^{-11}$ erg cm^{-2} counts^{-1} in 0.5–2 keV, and 2.22 and 0.85 $\times 10^{-11}$ erg cm^{-2} counts^{-1} in 2–10 keV, respectively. For each of the two energy bands, the exposure maps of the three instruments were co-added, weighted by their ECFs to create mosaics using the HEASoft `fcarith` tool and the SAS

emosaic task. The background maps were simulated after masking out the bright sources (with detection likelihood LIKE[6] > 4). The background map mosaics were then generated in the two energy bands. The source detection was performed on the mosaics of the three instruments using the SAS eboxdetect (with LIKE > 4) and emldetect (with LIKE > 6) tasks. The reliabilities of the chosen likelihood level correspond to 97.3 per cent in 0.5–2 keV and 99.5 per cent in 2–10 keV, respectively, according to the simulations of Cappelluti et al. (2007). The sources were detected simultaneously in the 0.5–2 and 2–10 keV energy bands, thus our catalogue contains sources with LIKE > 6 ($\geq 3\sigma$) in either 0.5–2 or 2–10 keV band, or the sources with the equivalent 0.5–10 keV detection likelihood[7] LIKE > 6. Our catalogue includes 165 sources: 88 sources with LIKE > 6 in 0.5–2 keV band and 71 sources with LIKE > 6 in 2–10 keV. The 2–10 keV flux lower limit of the sources with LIKE > 6 is $F_{2-10 \text{keV}} \approx 8 \times 10^{-15}$ erg cm^{-2} s^{-1}.

We cross-matched the *NuSTAR* catalogue with the *XMM–Newton* catalogue by using a radius combining a 20 arcsec matching radius and the positional error of *XMM–Newton* read from the emldetect best-fitting results in quadrature (a 1 arcsec systematic error was added to the *XMM–Newton* positional error in quadrature). The 20 arcsec matching radius is chosen to be three times of the best-fitting Rayleigh scale parameter of the input-output separations ($\sigma_{95\text{per cent}} = 6.3$ arcsec) from the simulations (see Fig. 7) to ensure that all potentially faint sources can be matched. 19 *NuSTAR* detected sources have *XMM–Newton* associations within the matching radius. *NuSTAR* source ID 31 has double *XMM–Newton* counterparts located 16.1 and 18.9 arcsec away from the *NuSTAR* detected position, although only one of these sources is detected with *Chandra* (see Section 5.1.2). The two *XMM–Newton* sources are in the opposite direction of the *NuSTAR* detected position. Therefore, *NuSTAR* might detect the combination of two soft X-ray sources.

One *XMM–Newton* detection (with 2–10 keV *likemin* = 13.7) is 21.5 arcsec away from *NuSTAR* source ID 6. The *NuSTAR* 3–24 keV flux of ID 6 is $F_{3-24} = 5.5 \pm 1.1 \times 10^{-14}$ erg cm^{-2} s^{-1}. Another *XMM–Newton* detection (with 2–10 keV *likemin* = 27.1) is 23.7 arcsec away from *NuSTAR* source ID 27. The *NuSTAR* 3–24 keV flux of ID 27 is $F_{3-24} < 1.4 \times 10^{-14}$ erg cm^{-2} s^{-1}. The simulations of the input-output separation of faint sources with flux $F_{3-24} < 10^{-13}$ erg cm^{-2} s^{-1} suggest that 6.5 per cent out of the 28 detected faint sources, which is ∼2 sources, might have a >20 arcsec distance between the *NuSTAR* and the soft X-ray detected coordinates (see Fig. 7). Furthermore, the 3–8 keV *NuSTAR* fluxes of ID 6 and ID 27 and the 3–8 keV flux of the two aforementioned *XMM–Newton* detections are consistent with the simulations of input–output fluxes distribution as shown in Fig. 11. Therefore, we associate the two *XMM–Newton* detections as the soft X-ray counterpart of ID 6 and ID 27. Thus, a total of 21 *NuSTAR* sources have detected *XMM–Newton* counterparts.

The 2–10 keV fluxes and flux errors (1σ) of the *XMM–Newton* detections were computed using the emldetect task if the 2–10 keV maximum likelihood of the sources is DET ML >6. For sources whose 2–10 keV maximum likelihood is DET ML <6, we
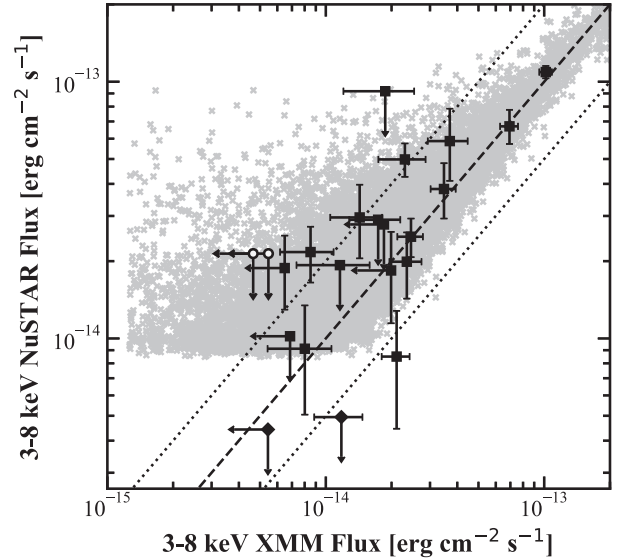
Figure 11. Comparison between 3–8 keV fluxes measured in *NuSTAR* and in *XMM–Newton*. The dashed line represents the 1:1 relation, while the dotted lines are a factor of two from the 1:1 relation. ID 30 and 33 and are plotted as the black diamonds. The black open circles are the two *XMM–Newton* counterparts of *NuSTAR* ID 31. The grey crosses on the background are the input and output fluxes from the simulations of the sources detected and above the 95 per cent reliability threshold.
in the 3–8 keV band. The 3–8 keV *NuSTAR* fluxes of sources that are not detected in S band are plotted as upper limits.

report the 90 per cent upper limit of the flux using the same equation as described in Section 4. We plot the 3–8 keV *NuSTAR* and *XMM–Newton* fluxes of the matched sources in Fig. 11. *NuSTAR* ID 31 has two potential *XMM–Newton* counterparts, so we plotted the fluxes of both *XMM–Newton* counterparts. The relations between the *NuSTAR* and *XMM–Newton* fluxes of most sources are consistent with the expectation from the simulations (see Fig. 8). The *NuSTAR* 3–8 keV flux of ID 30 and 33 are below the simulations because they are only detected above the threshold in the hard band. Nevertheless, their 3–8 keV flux upper limits are consistent with the *XMM–Newton* ones within a factor of two.

The *XMM–Newton* source number density at the flux limit of the *XMM–Newton* observation ($F_{3-8 \text{keV}} \sim 5 \times 10^{-15}$ erg cm^{-2} s^{-1}) is 390 deg^{-2}. The number of XMM–Newton sources found by chance within the search area (with a radius of 20 arcsec) around each *NuSTAR* source is <0.09. Therefore, all the matches are very likely to be real associations. We investigate the *NuSTAR* detected sources that do not have *XMM–Newton* cross-matched associations. Two sources (ID 26 and 28) are either out of the FoV of *XMM–Newton* or on the gaps between the detectors of *XMM–Newton*. SDSS J172421.74 + 654847.5 ($z = 0.833$ measured by Double Spectrograph (DBSP) of the Palomar Observatory, ATel # 12049) was a variable AGN discovered in the *Chandra* observations in 2018 (ATel # 11906), which is 27.1 arcsec away from *NuSTAR* ID 16. We found that ID 16 is also a variable source and its 3–8 keV *NuSTAR* flux in epoch one was consistent with the *Chandra* measured flux in July 2018. We thus associate this *Chandra* detected transient to *NuSTAR* ID 16. ID 16 was not detected by *XMM–Newton* in 2020 October as we expected it to be too faint (see its flux variabilities as a function of time in the upper panel of Fig. 17). The details of the flux variability of this source are discussed in Section 6.2.

ID 3, 5, 10, 15, 19, and 20 were detected in 3–8 keV band of *NuSTAR* with reliability of 79, 78, 99.5, 99.96, 96.4, and 89 per cent, but were not detected by *XMM–Newton*. These sources could be variable sources, whose flux decreased significantly in less than a year (sources with significant variability in fluxes were found in days to months in previous works, e.g. Risaliti, Elvis & Nicastro 2002; Markowitz, Krumpe & Nikutta 2014). They could also be spuriously detected sources by *NuSTAR*, although we note that only ∼2 spuriously detected sources are expected in the *NuSTAR* 95 per cent reliability catalogue. ID 23, 25, and 32 were neither detected in the soft band by *NuSTAR* nor by *XMM–Newton*. Therefore, they might be nearby heavily obscured sources whose soft X-rays are significantly suppressed due to large obscuration, which is supported by their high hardness ratio computed in Section 5.6. Since they do not have measured redshifts, we cannot exclude the possibility that they are spurious detections. Another possibility of the non-detection of these sources is that their soft X-ray fluxes were below the detection capability of the 10 ks *XMM–Newton* observation. The forthcoming *NuSTAR* and *XMM–Newton* observations will help better locate the positions of these sources, which may result in more matches, and distinguish from the different scenarios.

5.1.2 Chandra

To obtain better positional accuracy of the *NuSTAR*-detected sources, we also perform source detection using the *Chandra* data. We selected the *Chandra* NEP observation, which was taken close to the *XMM–Newton* observation mentioned above to minimize the effect of variability. Therefore, a *Chandra* observation on 2020 September 21 (ObsID: 21651) with exposure of ∼20 ks was used. The *Chandra* observation covered an area of 17 arcmin × 17 arcmin, only ≈50 per cent of the total *NuSTAR* NEP field. The *Chandra* data were reduced using CIAO software package (Fruscione et al. 2006) version 4.12 and *Chandra* CALDB version 4.12.3. The source detection was performed using the wavdetect algorithm in the 0.5–7 keV band. The source image, exposure map, and PSF map were created by running the fluximage script. The images were binned with a pixel size of 4 arcsec on a side. The wavdetect algorithm was then run on each on-axis chip with scales of 1 and 2 pixels, assuming a false-positive probability threshold of 10^{-6}, equivalent to one possibly spurious detection in the FoV.

Thirty-nine sources were detected in *Chandra*, and 16 were matched with *NuSTAR* sources using a 20 arcsec search radius. All 16 sources have also been detected by *XMM–Newton*, although only one of the two *XMM–Newton* counterparts of ID 31 was detected by *Chandra*. Of the five sources which were detected by *XMM–Newton* but not by *Chandra*, ID 1, 24, 27, and 29 were out of the *Chandra* FoV, and ID 2 was weakly detected by *Chandra* with a signal-to-noise ratio of SNR = 3.55 at the coordinate of *XMM–Newton* detection. The two sources (ID 26 and 28) that were out of the FoV or on the detecter gaps of *XMM–Newton* were out of the FoV of *Chandra* as well. ID 16 was neither detected by *Chandra* in 2020 September. Complete *Chandra* associations of the *NuSTAR* detected sources will be built after the release of the *Chandra* NEP source catalogue (Maksym et al. in preparation), which will cover the entire *NuSTAR* area.

Therefore, a total of 22 *NuSTAR* sources have a soft X-ray counterpart from *XMM–Newton* and/or *Chandra*. The soft X-ray (*Chandra* if having *Chandra* counterpart, otherwise *XMM–Newton*) coordinates of the associated source are listed in Table A1. The positions of the soft X-ray counterparts of each *NuSTAR* sources are plotted in Fig. 2.

5.2 Optical counterparts

The *JWST* NEP Time-Domain Field has extensive multiwavelength coverage. We used two optical catalogues to match the *NuSTAR* detected sources: SDSS DR16 (Ahumada et al. 2020) and *Subaru* Hyper Suprime-Cam (HSC; observed as part of the HEROES survey, PI: Hasinger; image reduced by S. Kikuta, catalogue produced by C. Willmer using SEXTRACTOR). We applied a magnitude cut to the HSC catalogue by removing the detections with *i*-band magnitude (all magnitudes below are quoted on AB system) $m_i < 19$ since bright sources are saturated in HSC observations. We also removed sources with $m_i > 25.5$ in the HSC catalogue because faint sources with $m_i > 25.5$ are likely beyond the detection capability of *NuSTAR*-NEP survey at $F_{3-8} = 8 \times 10^{-15}$ erg cm^{-2} s^{-1}. The HSC observation covered the entire *NuSTAR* observed field. SDSS is able to detect bright sources ($m_i < 19$) with accurately measured magnitude, while HSC is capable of detecting faint sources.

We only matched the optical catalogues with the 22 *NuSTAR* sources that have soft X-ray counterparts and thus better positional accuracy. The optical and IR properties of the rest 11 soft X-ray non-detected sources will be studied when further soft X-ray data are available. If the *NuSTAR*-detected sources have *Chandra* counterparts, the *Chandra* detected coordinates were used to match the optical and IR catalogues using a 3 arcsec search radius (see e.g. fig. 2 in Marchesi et al. 2016a). Otherwise, the *XMM–Newton* detected coordinates were used to match the optical and IR catalogues with a 4.5 arcsec search radius (corresponding to separations between the *XMM–Newton* detected coordinates and optical and IR associations' coordinates of 95 per cent of the *XMM–Newton* STRIPE 82 sources; LaMassa et al. 2016). Twenty *NuSTAR* sources (except ID 1 and ID 29) have at least one optical counterpart within the search radius of soft X-ray-detected coordinates. Fourteen sources have a unique optical counterpart. ID 31 has two soft X-ray counterparts, but only one of them has an optical source within the search radius. ID 16, 21, and 27 have two or three optical sources (only one of them is detected by SDSS) within the search radius. We assume that the SDSS detected sources are the most likely optical counterparts of ID 16, 21, and 27 because they are magnitudes brighter than the other HSC detected sources and are the closest to the soft X-ray position.[8]

ID 6 has one HSC source detected within the search radius with $m_i = 23.17$ which is $D = 1.6$ arcsec away from the soft X-ray-detected coordinate. However, a bright SDSS source with $m_i = 19.22$ is also close to the soft X-ray detected coordinate with $D = 3.6$ arcsec. Although the SDSS source is outside the search radius from the soft X-ray detected coordinate, it is closer to the *NuSTAR* detected coordinate. Therefore, we associated both optical sources with ID 6 and report both in the catalogue. ID 9 has two optical sources within the search radius: a SDSS source with $m_i = 18.80$ and $D = 2.8$ arcsec, and a HSC source with $m_i = 22.78$ and $D = 0.6$ arcsec. We cannot distinguish the optical counterpart of ID 9 because the brighter one is further from the soft X-ray-detected coordinate. Therefore, we consider both optical sources as possible counterparts of ID 9. ID

---

[8]The distances between soft X-ray positions and SDSS positions of the three sources are 0.3, 1.1, and 2.6 arcsec, respectively. The distances between soft X-ray positions and HSC positions of the three sources are 2.5, 2.5, 3.3, and 4.5 arcsec (ID 27 have two HSC detections within the searching radius), respectively.

33 has two HSC sources within the search radius with $m_i = 22.32$ and 22.58 and $D = 2.2$ and 2.6 arcsec, respectively. Therefore, we associate both HSC sources with ID 33.

No optical sources are within the search radius of the soft X-ray counterparts of ID 1 and 29. However, more than 10 SDSS and HSC sources are within their 20 arcsec of the *NuSTAR* detected coordinate. Therefore, we did not associate any optical source with ID 1 and 29 for now. The detection of ID 1 and 29 in the 2–10 keV band by *XMM–Newton* is $\sim 3\sigma$. A better measurement of the X-ray coordinates of ID 1 and 29 will be obtained after all accepted *NuSTAR* (for Cycle 6), *XMM–Newton* (together with Cycle 6 *NuSTAR* observations), and *Chandra* (Maksym in preparation) observations are completed and analysed. Thus, may match more optical counterparts using their better measured soft X-ray coordinates. Another possibility is that the optical counterpart of ID 29 is fainter than the optical catalogue limit based on its faint soft X-ray flux and the X-ray to optical relation discussed in Section 5.4.

Therefore, seventeen sources have a single optical counterpart, and three sources have double optical counterparts. Sixteen sources have SDSS counterparts, and six (ID 4, 6, 7, 17, 22, and 24) of them have SDSS measured photometric redshifts. ID 18 has SDSS spectroscopically measured redshift. ID 16 has DBSP spectroscopically measured redshift.

5.3 Infrared counterparts

We searched for IR counterparts to the soft X-rays detected *NuSTAR* sources using the catalogue produced by C. Willmer using *MMT* Magellan infrared spectrograph (MMIRS; McLeod et al. 2012). The MMIRS observations covered a region of 15 arcmin × 15 arcmin in the *JWST* NEP Time-Domain Field, which covered ∼40 per cent of the *NuSTAR* observations. The observations were taken using four MMIRS filters (*YJHK*). 14 out of the 20 sources that have optical counterparts have IR counterparts, and the coordinates of the IR counterparts are consistent with those of the optical counterparts. The six sources which do not have IR counterparts are out of the MMIRS FoV.

Five sources (ID 4, 12, 13, 14, and 22) have *MMT*/Binospec (0.39–1 μm; Fabricant et al. 2019) spectroscopically measured redshifts. Therefore, 11 sources in total have spectroscopic and/or photometric redshifts. The SDSS photometrically measured redshifts of ID 4 and 22 are consistent with their *MMT*/Binospec spectroscopically measured redshifts. Based on the available optical and IR spectra, six out of seven sources are determined as AGN with one source being ambiguous. A detailed analysis of the optical and IR properties of the 33 sources will be studied when all of their optical/IR spectra are available in the future work. The MMIRS coordinates and *MMT*/Binospec measured redshifts are reported in Table A1.

We also matched with the AllWISE catalogue using the Wide-field Infrared Survey Explorer mission (*WISE*; Wright et al. 2010). The nominal PSF of *WISE* is ≈ 8 arcsec, which is larger than the matching radii of the *Chandra* and *XMM–Newton*. Therefore, it was used to match the soft X-rays detected coordinates for both *Chandra* and *XMM–Newton*. 18 out of the 20 sources that have optical counterparts have *WISE* counterpart with only three sources having separations $D > 3$ arcsec. ID 11 and 31, which lack *WISE* counterparts, have both optical ($m_i = 25.3$ and 21.7) and MMIRS (with *K*-band magnitudes of $m_K = 21.6$ and 21.3) counterparts, suggesting that they are beyond the sensitivity of *WISE*. The *WISE* coordinates of the 18 sources are reported in Table A1.

5.4 X-ray to optical properties

The X-ray–optical flux (*X/O*) ratio has been historically used to study the nature of X-ray detected sources (e.g. Maccacaro et al. 1988). The *X/O* ratio is defined as $X/O = \log(f_X/f_{opt}) = \log(f_X) + m_{opt}/2.5 + C$, where f_X is the X-ray flux in a given energy band, m_{opt} is the optical magnitude at a chosen band, and C is a constant depending on the energy bands chosen in the X-ray and optical observations. The *X/O* relation was initially studied using the soft X-ray fluxes, finding that most of the detected AGN in *Einstein*, *ROSAT*, and *ASCA* surveys can be characterized by $X/O = 0 \pm 1$ (Stocke et al. 1991; Schmidt et al. 1998; Akiyama et al. 2000).

We plotted the *i*-band (SDSS if the optical counterpart has SDSS measurement, otherwise *Subaru*/HSC measurement) magnitudes as a function of soft (3–8 keV) and hard (8–24 keV) X-ray fluxes in Fig. 12. The *X/O* ratios were calculated using constants of $C_{i, 3-8} = 5.49$ and $C_{i, 8-24} = 5.35$ for soft and hard band, respectively. The constants were computed taking into account the optical band used in NEP. Sources (ID 1 and 29) that do not have associated optical counterparts were not plotted in Fig. 12. ID 6, 9, and 33 have double optical associations, so we plotted the *i*-band magnitudes of both optical associations. The *i*-band magnitude of ID 8 measured by SDSS has uncommonly large uncertainties with $m_i = 23.38 \pm 0.97$, therefore, we use the HSC measured *i*-band magnitude for ID 8 which is $m_i = 22.33$.

Most of our sources lie in the $-1 < X/O < 1$ region, suggesting that they are AGN, which is consistent with what is found using their optical/IR spectra. High *X/O* ratio is found in ID 12 ($z = 0.8846$), which has $f_X/f_{opt} = 15.1^{+5.1}_{-4.7}$ and $27.8^{+5.8}_{-5.5}$ in 3–8 keV and 8–24 keV band, respectively. Another high *X/O* source (ID 11), which is also the optically faintest one in the sample, is a CT-AGN candidate. High (>10) *X/O* ratio sources were detected in previous *Chandra* and *XMM–Newton* surveys (Hornschemeier et al. 2001; Fiore et al. 2003; Civano, Comastri & Brusa 2005; Brusa et al. 2007; Laird et al. 2008; Xue et al. 2011) and *NuSTAR* surveys (Civano et al. 2015; Lansbury et al. 2017), which were associated with high redshift or large obscuration. We note that four out of five CT-AGN candidates (see Section 5.6) which have optical counterparts have $X/O > 0$. We also compared our results with the *NuSTAR* COSMOS sample (Civano et al. 2015) in Fig. 12. Both surveys showed that the majority of the *NuSTAR* detected sources are AGN with $-1 < X/O < 1$. The two surveys probe different parameter spaces on the X-ray–optical plane with NEP probing the lower X-ray flux regime while COSMOS probed the higher X-ray flux regime.

5.5 Luminosity–Redshift Distribution

In Fig. 13, we plotted the 10–40 keV rest-frame luminosities of the 11 *NuSTAR* NEP sources with redshift information as a function of their redshifts. The 10–40 keV rest-frame luminosities were computed by converting the 3–24 keV fluxes assuming a power law model with $\Gamma = 1.80$ and taking into account the different bandpasses due to the redshift effect. The plotted luminosities were not corrected for any intrinsic absorption. The 3–24 keV survey sensitivity at 20 per cent of the sky coverage is plotted. We detected a high-luminosity (10–40 keV flux of $2.4 \pm 0.1 \times 10^{45}$ erg s^{-1}) and high-redshift source (ID 18, a narrow-line Seyfert 1 galaxy, NLSy1, $z = 1.44$) in the *NuSTAR* NEP survey. In Fig. 13, we also present sources detected in previous *NuSTAR* surveys including the COSMOS (Civano et al. 2015), ECDFS (Mullaney et al. 2015), UDS (Masini et al. 2018a), and 40-month serendipitous (Lansbury et al. 2017) surveys. 99 per cent of the detected sources from previous *NuSTAR* surveys were sampled
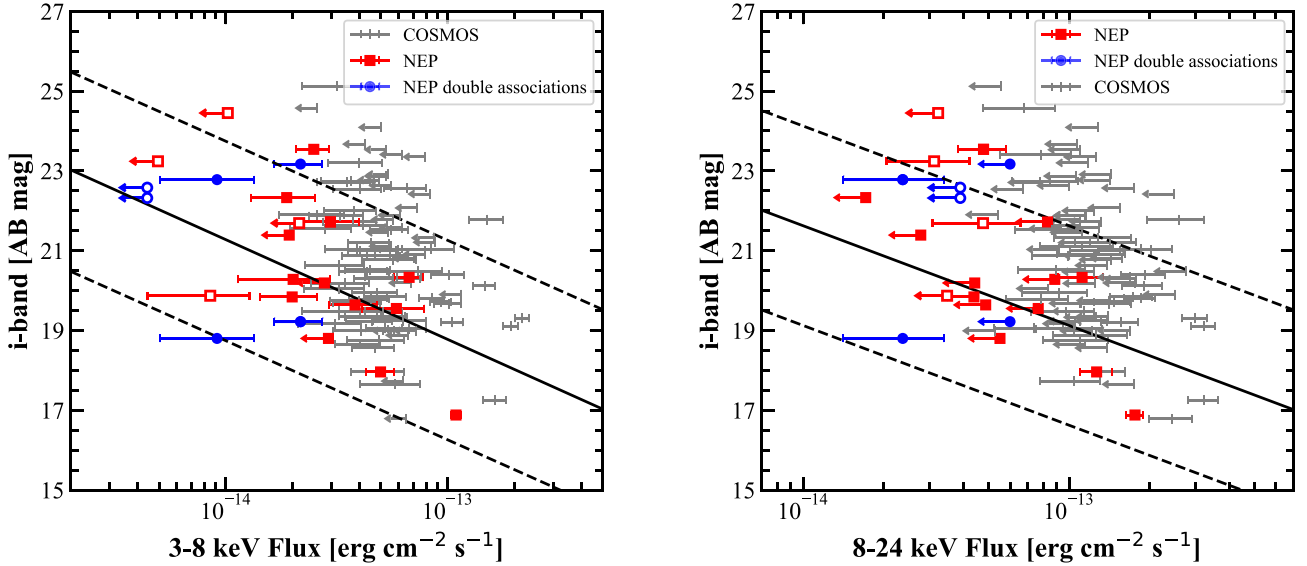
Figure 12. The *i*-band magnitude as a function of X-ray flux (left: 3–8 keV; right: 8–24 keV) of our sample. Sources with single optical counterparts are plotted in red squares and sources with double optical associations are plotted in blue circles. Candidate CT-AGN are labeled as open squares or circles. The solid and dashed lines represent the classical AGN locus (Maccacaro et al. 1988) when $X/O = 0 \pm 1$. We also compare the *NuSTAR* COSMOS sample (grey; Civano et al. 2015).
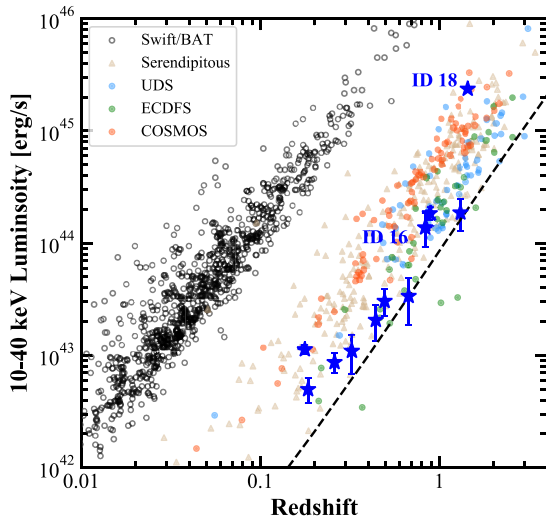
Figure 13. 10–40 keV rest frame luminosity versus redshift of the NEP *NuSTAR* sources (blue star). ID 18 (NLSy1) and ID 16 (*Chandra* detected transient) are labeled. The NEP survey sensitivity at 20 per cent of the sky coverage is plotted as dashed line. *NuSTAR* COSMOS (red circles; Civano et al. 2015), ECDFS (green circles; Mullaney et al. 2015), UDS (blue circles; Masini et al. 2018a), and serendipitous (brown triangles; Lansbury et al. 2017) surveys are presented as well. We also compare with the *Swift*-BAT 105-month sample (black open circles; Oh et al. 2018). The luminosities were not corrected for any intrinsic absorption.

above the NEP sensitivity line, reflecting that the NEP survey indeed reached the deepest sensitivity.

We also compared *NuSTAR* detected sources with the sources in the 105-month *Swift*-BAT catalogue (Oh et al. 2018) in Fig. 13. The 10–40 keV luminosities of the BAT detected sources were converted from the 14–195 keV luminosities reported in the *Swift*-BAT catalogue assuming a power law model with $\Gamma = 1.80$. The *Swift*-BAT and *NuSTAR* surveys are highly complementary. *Swift*-BAT samples large sky-area but with low sensitivity, while *NuSTAR* samples small areas

but with high sensitivity. *Swift*-BAT sampled AGN mostly in the local Universe (with median redshift at $<z_{BAT}> = 0.044$), while *NuSTAR* sampled higher redshift ($<z_{NuS}> = 0.734$) sources.

5.6 Hardness ratio

While detailed spectral analysis will be reported in a further publication, to give an estimate of the obscuration of the *NuSTAR* NEP sample, we computed the hardness ratio of each detected source in the sample using the Bayesian estimation of hardness ratios method (BEHR; Park et al. 2006). Here, the hardness ratio is defined as HR $= (H-S)/(H+S)$, where H and S are the net counts in the 8–24 keV and 3–8 keV bands, respectively. The BEHR method calculates the mean, median, and mode location of the hardness ratio distribution for each source and the uncertainties of these values (we report the mode value and its uncertainty in the catalogue), especially for astrophysical sources in the Poisson regime of low counts. The 1σ error of the hardness ratio is calculated either by Gaussian quadrature numerical integration method if the number of net counts of the hard or soft energy bands is less than 15, or by the Gibbs sampler method for a larger number of net counts. The differences in the effective exposure time between the two energy bands were also considered in the calculation.

In the upper panel of Fig. 14, the hardness ratio of 33 sources are compared to the expected values of spectral models. The model assumes an absorbed power-law with slope of $\Gamma = 1.80$ and intrinsic absorption of $N_H = 10^{20}$ and 10^{24} cm^{-2} separately. The models are computed assuming different redshifts: $z = 0$, and $z = 0.734$, which is the median redshift of the sources detected in previous *NuSTAR* surveys, see Section 5.5. We note that the upper limits of the hardness ratio of seven sources are below the $N_H = 10^{20}$ cm^{-2} model predictions, which might suggest significant soft excess in these sources. The hardness ratio is sensitive to obscuration of $N_H > 10^{23}$ cm^{-2} (e.g. Masini et al. 2018a). The relation between the hardness ratio and the obscuration of the source depends on the redshift. Therefore, we plotted the hardness ratio of the 11 sources which have single spectroscopically or photometrically measured
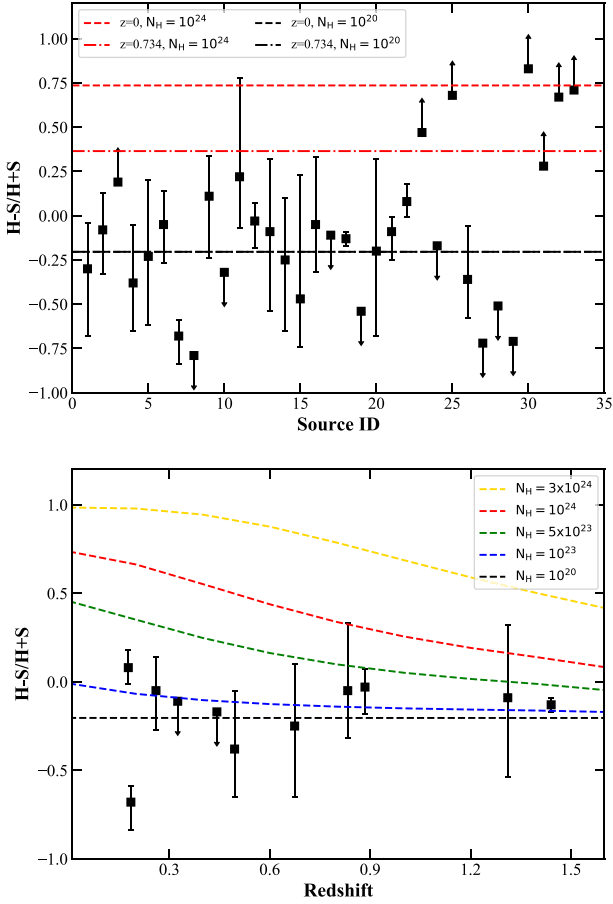
Figure 14. Upper: Hardness ratios (with 1σ errors) of the 33 sources in the 95 per cent reliability catalogue. Expected values of spectral models of $N_H = 10^{24}$ cm^{-2} (red) and 10^{20} cm^{-2} (black) at $z = 0$ (dashed line) and $z = 0.734$ (dash–dot line) are plotted. The expected values of 10^{20} cm^{-2} at two redshifts are similar, so that the two lines overlap. Lower: Hardness ratio (with 1σ errors) as a function of redshift. Dashed lines show the expectations using absorbed power law models with $\Gamma = 1.80$ and different intrinsic column densities of 3×10^{24}, 10^{24}, 5×10^{23}, 10^{23}, and 10^{20} cm^{-2} (from top to bottom) as a function of redshift.

redshifts as a function of their redshifts in the lower panel of Fig. 14. We also plotted ID 6 in the lower panel of Fig. 14 assuming the redshift measured in one of its double optical and IR counterparts. The hardness ratio values of each source is reported in Table A1.

ID 30 has a hardness ratio lower limit of 0.83, which is above the CT threshold even for $z = 0$. Therefore, ID 30 is a candidate CT-AGN despite lacking redshift information. For five sources without redshift (ID 3, 23, 25, 31, 32, and 33), their hardness ratio are above the CT threshold assuming a median redshift $z = 0.734$, making them CT-AGN candidates. The hardness ratio upper limits of ID 11 (even for $z = 0$) and ID 13 ($z = 1.311$) are above the CT threshold, as shown in the lower panel of Fig. 14. Therefore, they are also CT-AGN candidates. Details about these CT-AGN candidates and the CT-AGN fraction are discussed in Section 6.1.

We computed the hardness ratio of XMM-*Newton* detected sources using the 2–10 keV and 0.5–2 keV bands fluxes. The hardness ratios measured in XMM-*Newton* are compared with those measured in *NuSTAR* in Fig. 15. ID 31 has two XMM-*Newton* counterparts, so both of them are plotted in the figure. Most of the sources which are measured as obscured or unobscured AGN by *NuSTAR*
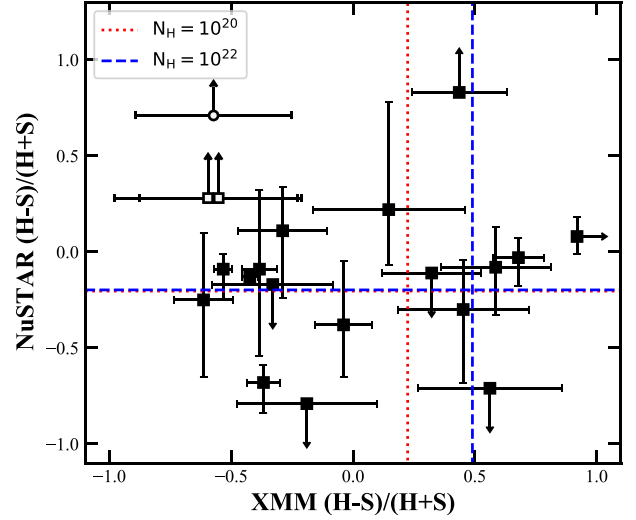
Figure 15. *NuSTAR* hardness ratio (with 1σ errors) as a function of their XMM-*Newton* counterpart hardness ratio (with 1σ errors). Expected hardness ratio values of spectral models of $N_H = 10^{20}$ cm^{-2} (red dotted line) and 10^{22} cm^{-2} (blue dashed line) at $z = 0.734$ of *NuSTAR* and XMM-*Newton* are plotted. ID 31 has two XMM-*Newton* counterparts, and they are plotted in open squares. ID 33 is plotted in open circle.

are also measured as obscured or unobscured by XMM-*Newton* within uncertainties (in the upper right and lower left corners of Fig. 15). ID 33 is detected as heavily obscured AGN by *NuSTAR* but is determined as unobscured AGN by XMM-*Newton* in the upper left of the figure. However, ID 33 could still be considered a possible CT-AGN candidate, given the simple spectral model used in categorizing the sources. For instance, ID 33 might have strong non-AGN thermal emissions at <2 keV, so that its XMM-*Newton* hardness ratio is significantly soft. Follow-up spectral analysis of the sources with enough counts will be used to determine the spectral parameters (slope and obscuration at minimum).

6 DISCUSSION

6.1 CT Fraction

As discussed in Section 5.6, ID 30 is a good CT-AGN candidate. Therefore, the lower limit of the CT-AGN fraction of the NEP 95 per cent catalogue is 1/33 ∼3 per cent. The mode values of hardness ratio of five sources are above the CT threshold if their redshifts are assumed to be $z = 0.734$. Thus, the expected CT fraction of the catalogue is 7/33 ∼21 per cent. The hardness ratio upper limits of the two sources are above the CT threshold. Therefore, the upper limit of CT-AGN fraction is 9/33 ∼27 per cent. As a result, the observed CT fraction of the NEP 95 per cent reliability catalogue is 21^{+6}_{-18} per cent at 1σ confidence level. The CT fraction of the NEP survey will be better constrained when all sources have redshift measurements with the future *JWST* and *J-PAS* observations. We note that the nine CT candidates were not significantly detected in the *NuSTAR* soft (3–8 keV) band (except for ID 13) and they were neither detected by XMM-*Newton* (except for ID 30).

The observed CT fraction measured in the NEP field is consistent with the CT fraction measured in the *NuSTAR* COSMOS sample (13 per cent–20 per cent; Civano et al. 2015), which was estimated using the hardness ratio as well. Masini et al. (2018a) computed the CT fraction of the *NuSTAR* UDS sample, which is
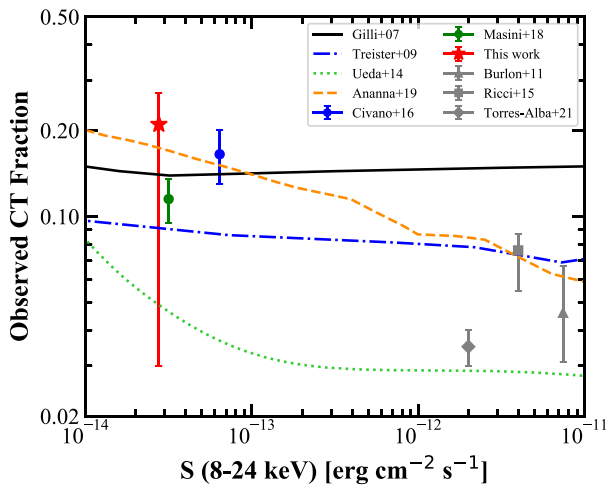
Figure 16. Observed CT fraction as a function of 8–24 keV flux. The CT fraction measured by *NuSTAR* in NEP field is plotted as a red star at the 8–24 keV survey sensitivity at 20 per cent of the sky coverage. Blue and green circles are the *NuSTAR* measurements in COSMOS (Civano et al. 2015) and UDS (Masini et al. 2018a) fields. Grey triangle, square, and diamond are the *Swift*-BAT measurements by Burlon et al. (2011), Ricci et al. (2015), and Torres-Albà et al. (2021). We compared with the CT fractions predicted by the CXB population synthesis models with Gilli et al. (2007) (black solid line), Treister et al. (2009) (blue dash–dotted line), Ueda et al. (2014) (green dot line), and Ananna et al. (2019) (orange dashed line).

11.5 per cent±2.0 per cent by performing spectral analysis. The result in the UDS field is in agreement with the lower limit of the NEP and COSMOS field, although they used different methods when estimating the N_H values. Masini et al. (2018a) reported that the CT fraction measured in the conservative sample (99 per cent reliability catalogue, $f_{CT, 99} \sim 3$ per cent±2 per cent) is significantly lower than their 97 per cent reliability catalogue. However, this significant drop of the CT fraction is not found in the NEP field, where the CT fraction in our 99 per cent reliability catalogue is [5 per cent–24 per cent]. Burlon et al. (2011) and Ricci et al. (2015) found a CT fraction of ∼4.6 per cent–7.6 per cent using the *Swift*-BAT sample. A recent work (Torres-Albà et al. 2021), which analysed the CT-AGN candidates in the BAT sample using high-quality *NuSTAR* observations, found a lower CT fraction of the BAT sample of 3.5 per cent±0.5 per cent.

The observed CT fraction obtained in this work and the other *NuSTAR* and *Swift*-BAT measurements are plotted in Fig. 16. We also compare with the CT fractions predicted by the population synthesis model of CXB (Gilli et al. 2007; Treister et al. 2009; Ueda et al. 2014; Ananna et al. 2019) in Fig. 16. The recent Ananna et al. (2019) model are in good agreement with the hard X-ray observed CT-AGN fraction at both bright and faint fluxes.

We detected one good CT-AGN candidate (ID 30) and two possible CT-AGN candidates (ID 13 and 31) in the 8–24 keV band, which are above the 95 per cent reliability threshold. This is consistent with the CXB population synthesis models, which predicted 2 (Gilli et al. 2007) or 0.7 (Ueda et al. 2014) CT-AGN being detected in the 8–24 keV band, respectively. The CT fraction reported in this work is the observed one. An estimation of the intrinsic CT fraction based on our sample is beyond the scope of this paper and further X-ray spectral analysis as well as a large number of photometric and spectroscopic redshifts will allow a better estimate of obscuration and CT fraction. The spectrum of each source will be analysed using Markov chain Monte Carlo (MCMC) parameter estimation techniques as described

in Lanzuisi et al. (2018) in a further work and the full obscuration probability distribution function (PDF) will be used to derive the true CT fraction.

6.2 Variability analysis

Variability of high redshift ($z > 0.5$) AGN has been studied in deep *Chandra* and XMM-*Newton* extragalactic surveys (e.g. Lanzuisi et al. 2014; Yang et al. 2016; Paolillo et al. 2017). However, such studies have not been performed in hard X-ray band. The *JWST* NEP field is a new effort to study the time-domain astrophysics and the *NuSTAR* NEP survey was designed to have variability as its primary focus. The field was observed in three epochs during October 2019, January 2020, and March 2020.

Among the 33 detected sources, 8 sources were observed only in one epoch, 14 sources were observed in two epochs, and 11 sources were observed in all three epochs. To study the variability properties of the 25 sources observed in multiple epochs, we computed their vignetting corrected count rates as a function of time in five energy bands. The observation data (FPMA + FPMB), simulated background, and exposure map of the three observations in a given epoch were merged into mosaics. We extracted the total and background counts on the observation and background mosaics at the coordinate of each *NuSTAR* detection using a circular aperture of 20 arcsec radius in each epoch. The count rates were then computed by dividing the net counts by the vignetting-corrected exposure time in a given energy band for each epoch. Therefore, the count rate has taken into account the variations in the vignetting correction among different epochs of observations. The net count errors were computed using equations (9) and (12) in Gehrels (1986) at 90 per cent confidence level.

The variability is determined by using the differences of the count rates of the source in different epochs and compare these with the combined errors of the count rates in different epochs (e.g. $Err_{cob} = (Err_1^2 + Err_2^2)^{1/2}$). At 90 per cent confidence level, six sources (ID 3, 4, 6, 13, 19, and 20) exhibited only short-term variability between epoch one and epoch two (2 months) or/and between epoch two and epoch three (3 months) in 3–24 keV. Six sources (ID 15, 16, 22, 23, 24, and 29) exhibited only long-term variability between epoch one and epoch three (five months). Four sources (ID 12, 17, 18, and 32) exhibited both long-term and short-term variabilities. Therefore, among the 25 sources observed in multiple epochs, 16 sources showed variability in the short term or/and long term. This is in agreement with what was found in the 15 yr *Chandra* Deep Field-South observations that 74 per cent of the sources in the survey showed flux variability (Yang et al. 2016).

SDSS J172421.74 + 654847.5 (ID 16) is a variable AGN found in *Chandra* observations, whose flux was found to increase by a factor of ∼7 from April 11 to July 26 in 2018 but then decreased by 25 per cent on July 31 (ATel # 11906 and ATel # 12049). The source flux was computed by fitting its *Chandra* spectra. *NuSTAR* observed this source twice in 2019 October and 2020 March. We found that the 3-8 keV flux of this source was higher than the *Chandra* detected flux in 2019 October, but decreased by ∼74 per cent in 2020 March. The *NuSTAR* flux was computed by converting its count rates measured in each epoch using the count-rate-to-flux CF (3.39×10^{-11} erg cm^{-2} counts^{-1}). We present the 3–8 keV flux as a function of time in the upper panel of Fig. 17. XMM-*Newton* did not detect this source, so we plot an upper limit of flux 8×10^{-15} erg cm^{-2} s^{-1} (2–10 keV flux limit of the XMM-*Newton* detection). In the lower panel of Fig. 17, we also presented its count rates in the two *NuSTAR* epoch in 3–24 keV, 3–8 keV, and 8–24 keV bands. We also found an increasing
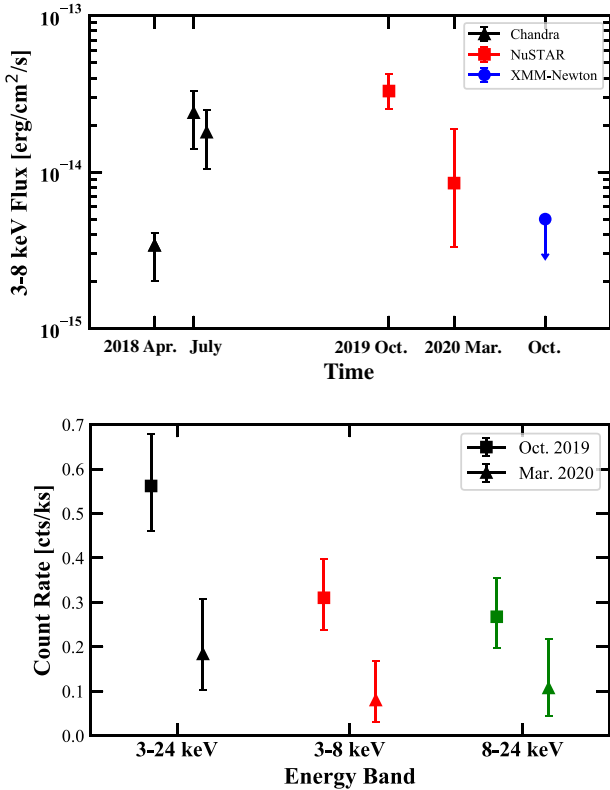
Figure 17. Upper: 3–8 keV flux of ID 16 (SDSS J172421.74 + 654847.5) as a function of time. *Chandra* and *NuSTAR* observations are labeled using black triangles and red squares, respectively. XMM-*Newton* didn't detect the source in Oct. 2020, so it is plotted as the upper limit (blue circle). The flux uncertainties are at 90 per cent confidence level. Lower: Vignetting corrected *NuSTAR* count rates of ID 16 in the two epochs (square for epoch 1 and triangle for epoch 2) in three energy bands.

X-ray absorption in ID 16 at $> 1\sigma$ confidence level. The HR of ID 16 in *NuSTAR* epoch 1 is $-0.05^{+0.32}_{-0.37}$ and $0.42^{+0.20}_{-0.10}$ in epoch 3. This significant variability of its HR suggests that X-ray absorption might play a significant role in the flux drop of ID 16. The source will be covered again by *NuSTAR* in cycle 6, which will enable us to better understand the flux and absorption variability of ID 16.

6.2.1 Source detection by epoch

When generating the source catalogue, we performed source detection on the mosaics of all three epochs' observations to achieve the deepest exposure. Variable sources, which were luminous in a single epoch, might be missed when performing source detection on the full mosaic. Therefore, to explore the existence of such events, we performed source detection on each epoch in five energy bands on FPMA + FPMB mosaics. Following the same source detection technique in Section 4, we created the 95 per cent reliability source catalogue for each epoch. We used the same DET ML–reliability relations in different exposure intervals obtained in Section 3.3. We computed the exposure map for each epoch. The area covered by each epoch are $0.080 \, \mathrm{deg}^2$, $0.097 \, \mathrm{deg}^2$ and $0.096 \, \mathrm{deg}^2$. The deepest vignetting-corrected exposure for each epoch reaches 337 ks, 351 ks, and 264 ks.

In epoch one, fourteen sources were detected above the 95 per cent reliability threshold. In the area covered by epoch one, twelve sources were detected in the total mosaic but were not detected in epoch

one, suggesting that the signal-to-noise (S/N) ratios of these sources were below the detection threshold in a single epoch. One of the sources detected in epoch one (ID E1–12) was not detected in the total mosaic. The effective exposure time of this source is 22 ks and it was only detected above 95 per cent reliability threshold in 3–24 keV (DET ML = 13.10). We did not find any *XMM–Newton* and *Chandra* counterparts of ID E1–12. The position of ID E1–12 was also observed in epoch three, but no source was detected within 30 arcsec of its position. Therefore, ID E1–12 might be a spurious detection due to background fluctuation, although we cannot exclude the possibility that the source was only bright in epoch one so that we did not detect it in epoch three and *XMM–Newton* and *Chandra* observations.

In epoch two, we detected fourteen sources above the 95 per cent reliability threshold. In the area covered by epoch two, eleven sources were detected in the total mosaic but not in epoch two. One of the sources detected in epoch two (ID E2–14) was not detected in the total mosaic. The effective exposure time of this source is 139 ks and it was only detected above 95 per cent reliability threshold in 3–8 keV (DET ML = 11.87). We did not find any *XMM–Newton* and *Chandra* counterparts of ID E1–12. The position of ID E2–14 was also observed in epoch one and three, but no source was detected within 30 arcsec of its position. The source was close to (37 arcsec separation) the brightest source (ID 18, the NLSy1) in the FoV of the survey. Therefore, ID E2–14 might be a spurious detection since it was on the edge of the PSF of a bright source.

We only detected ten sources above the 95 per cent reliability threshold in epoch three due to its lower exposure time compared to epochs one and two. In the area covered by epoch three, eleven sources were detected in the total mosaic but not in epoch three. One of the sources detected in epoch three (ID E3–6) was not detected in the total mosaic. The effective exposure time of this source is 165 ks and it was only detected above 95 per cent reliability threshold in 3–24 keV (DET ML = 12.79). We found a soft X-ray counterpart of ID E3–6 detected by *Chandra* (D = 17.3 arcsec). *XMM–Newton* also detected a source close to ID E3–6 but with D = 21.6 arcsec. One HSC (m_i = 24.7) source was associated with ID E3–6 using the *Chandra* coordinate. The position of ID E3–6 was also observed in epoch one, but it was not detected. Therefore, ID E3–6 might be a variable source, which was dim in epoch one but became luminous in *NuSTAR* epoch three, *XMM–Newton* and *Chandra* observations.

This preliminary study of source variability among epochs shows that *JWST* NEP Time-Domain Field is a field rich in variable events. An overall analysis of the variable sources is out of the scope of this paper. We will perform a comprehensive study of the X-ray variability in the *JWST* NEP Time-Domain Field when all observations are completed including 4 epochs of *NuSTAR* observations in Cycle 6, together with long term soft X-ray observations in the same field. The study will include but is not limited to continuous monitoring of the discovered variable sources, studying the 3–8 keV and 8–24 keV light curves of the sources, and analysing the hardness ratio variability of each source among different epochs of observations.

7 CONCLUSION

In this paper, we presented the *NuSTAR* survey of the *JWST* NEP Time-Domain Field, which is one of the most sensitive *NuSTAR* surveys. The initial survey consists of nine observations conducted

in three epochs from September 2019 to March 2020 with a total exposure time of 681 ks and covers an area of ~0.16 deg^2.

(i) We detected 21 sources above the 99 per cent reliability threshold and 33 sources above the 95 per cent reliability threshold in the *NuSTAR* survey of the *JWST* NEP Time-Domain Field. The source detection was performed in six energy bands including 3–24 , 3–8, 8–24, 8–16, 16–24, and 35–55 keV. The distribution of the detected sources in the 95 per cent reliability catalogue is listed in Table 3. Only one source was detected in 16–24 keV band, and no source was detected in 35–55 keV band. We focused our analysis on the 95 per cent reliability catalogue, in which we statistically expect only ~2 spurious detections.

(ii) We computed the log$N$–log$S$ of 3–8, 8–24, and 8–16 bands, which are presented in Fig. 10. The lower limits of the 3–8 keV number counts obtained in our work are consistent with the measurements of previous *NuSTAR* and soft X-ray surveys and the constraints from the CXB population synthesis models. The number counts of 8–24 and 8–16 keV bands are in good agreement with previous *NuSTAR* measurements and the constraints of the CXB population synthesis models.

(iii) We analysed two soft X-ray (10 ks *XMM–Newton* and 20 ks *Chandra*) observations taken in 2020, which covered about 90 per cent of the *NuSTAR* field. We found that 22 *NuSTAR* sources have a soft X-ray counterpart detected by *XMM–Newton* and/or *Chandra*. The *NuSTAR* sources which do not have soft X-ray counterpart might be the sources not covered by the soft X-ray observations, faint sources below the detection capability of the soft X-ray observations, variable sources, heavily obscured AGN, or spurious detections.

(iv) We explored the X-ray-optical properties of the *NuSTAR*-detected sources. The *i*-band magnitude of the sources as a function of their 3–8 and 8–24 keV fluxes are plotted in Fig. 12. Most of the detected sources are in the locus of *X/O* = 0 ± 1, suggesting that they are AGN, which is consistent with what is found using their optical and IR spectra. Pervious *NuSTAR* extragalactic surveys also showed that the detected sources are dominated by AGN, but the NEP survey reaches a deeper X-ray flux.

(v) Eleven sources have measured redshifts. Their luminosities versus redshifts are plotted in Fig. 13, showing that the *NuSTAR* NEP survey is one of the most sensitive survey among *NuSTAR* contiguous surveys to date. The brightest source detected in the *NuSTAR* NEP survey is a NLSy1 ($z = 1.44$) and the spectral analysis of this source alone will be presented in Zhao et al. (in preparation).

(vi) We computed the hardness ratio of each source and plotted them in Fig. 14. We found that one sources is a good CT-AGN candidate, and eight sources are possible CT-AGN candidates. The CT fraction of the whole sample is 21^{+6}_{-18} per cent at 1σ confidence level, which is consistent with the results of previous *NuSTAR* surveys. The uncertainties on the CT fraction will be significantly reduced when the redshifts of all sources in the catalogue are measured. A broadband X-ray spectral analysis of all detected sources will be presented in a future work.

(vii) The survey was designed to have variability as its prime focus, and our study has shown that the *JWST* NEP Time-Domain Field is indeed rich in variable sources. 16 out of the 25 sources observed in multi-cycles showed variabilities at 90 per cent confidence level in 3–24 keV band. We also performed source detection by epoch and found three new sources which were not detected in the mosaics combining all observations. A further comprehensive variability study will be conducted after all observations approved in *NuSTAR* cycle 6 are taken.

DATA AVAILABILITY

The electronic version of the generated 95 per cent reliability catalogue can be found on VizieR.

REFERENCES

Ahumada R. et al., 2020, ApJS, 249, 3
Aird J. et al., 2015, ApJ, 815, 66
Akiyama M. et al., 2000, ApJ, 532, 700
Ananna T. T. et al., 2019, ApJ, 871, 240
Bertin E., Arnouts S., 1996, A&AS, 117, 393
Brunner H., Cappelluti N., Hasinger G., Barcons X., Fabian A. C., Mainieri V., Szokoly G., 2008, A&A, 479, 283
Brusa M. et al., 2007, ApJS, 172, 353
Burlon D., Ajello M., Greiner J., Comastri A., Merloni A., Gehrels N., 2011, ApJ, 728, 58
Cappelluti N. et al., 2007, ApJS, 172, 341
Cappelluti N. et al., 2009, A&A, 497, 635
Cappelluti N. et al., 2017, ApJ, 837, 19
Chen C.-T. J. et al., 2018, MNRAS, 478, 2132
Civano F. et al., 2015, ApJ, 808, 185
Civano F. et al., 2016, ApJ, 819, 62
Civano F., Comastri A., Brusa M., 2005, MNRAS, 358, 693
Elvis M. et al., 2009, ApJS, 184, 158
Fabricant D. et al., 2019, PASP, 131, 075004
Fiore F. et al., 2003, A&A, 409, 79

Fruscione A. et al., 2006, in Silva D. R., Doxsey R. E., eds, Society of Photo-Optical Instrumentation Engineers (SPIE) Conference Series, p. 62701V

Gandhi P., Horst H., Smette A., Hönig S., Comastri A., Gilli R., Vignali C., Duschl W., 2009, A&A, 502, 457

Gardner J. P. et al., 2006, Space Sci. Rev., 123, 485

Gehrels N., 1986, ApJ, 303, 336

Gilli R., Comastri A., Hasinger G., 2007, A&A, 463, 79

Harrison F. A. et al., 2013, ApJ, 770, 103

Harrison F. A. et al., 2016, ApJ, 831, 185

Hasinger G. et al., 2007, ApJS, 172, 29

HI4PI Collaboration et al., 2016, A&A, 594, A116

Hickox R. C., Markevitch M., 2006, ApJ, 645, 95

Hornschemeier A. E. et al., 2001, ApJ, 554, 742

Jansen R. A., Windhorst R. A., 2018, PASP, 130, 124001

Laird E. S. et al., 2008, ApJS, 180, 102

LaMassa S. M. et al., 2016, ApJ, 817, 172

Lansbury G. B. et al., 2017, ApJ, 836, 99

Lanzuisi G. et al., 2014, ApJ, 781, 105

Lanzuisi G. et al., 2018, MNRAS, 480, 2578

Luo B. et al., 2016, ApJS, 228, 2

Maccacaro T., Gioia I. M., Wolter A., Zamorani G., Stocke J. T., 1988, ApJ, 326, 680

Marchesi S. et al., 2016a, ApJ, 817, 34

Marchesi S. et al., 2016b, ApJ, 830, 100

Markowitz A. G., Krumpe M., Nikutta R., 2014, MNRAS, 439, 1403

Masini A. et al., 2018a, ApJS, 235, 17

Masini A. et al., 2018b, ApJ, 867, 162

McLeod B. et al., 2012, PASP, 124, 1318

Merloni A., Heinz S., 2008, MNRAS, 388, 1011

Miyaji T. et al., 2015, ApJ, 804, 104

Mullaney J. R. et al., 2015, ApJ, 808, 184

Oh K. et al., 2018, ApJS, 235, 4

Padovani P. et al., 2017, A&AR, 25, 2

Paolillo M. et al., 2017, MNRAS, 471, 4398

Park T., Kashyap V. L., Siemiginowska A., van Dyk D. A., Zezas A., Heinke C., Wargelin B. J., 2006, ApJ, 652, 610

Pineau F.-X. et al., 2017, A&A, 597, A89

Ricci C., Ueda Y., Koss M. J., Trakhtenbrot B., Bauer F. E., Gandhi P., 2015, ApJ, 815, L13

Risaliti G., Elvis M., Nicastro F., 2002, ApJ, 571, 234

Schmidt M. et al., 1998, A&A, 329, 495

Siemiginowska A., Civano F., 2019, in Wilkes. B., Tucker W., eds, The Chandra X-ray Observatory. IOP Publishing, p. 8

Soltan A., 1982, MNRAS, 200, 115

Stocke J. T., Morris S. L., Gioia I. M., Maccacaro T., Schild R., Wolter A., Fleming T. A., Henry J. P., 1991, ApJS, 76, 813

Torres-Albà N. et al., 2021, preprint (arXiv:2109.00599)

Treister E., Urry C. M., Virani S., 2009, ApJ, 696, 110

Ueda Y., Akiyama M., Hasinger G., Miyaji T., Watson M. G., 2014, ApJ, 786, 104

Vasudevan R. V., Mushotzky R. F., Gandhi P., 2013, ApJ, 770, L37

Vito F. et al., 2017, MNRAS, 473, 2378

Wik D. R. et al., 2014, ApJ, 792, 48

Wright E. L. et al., 2010, AJ, 140, 1868

Xue Y. Q. et al., 2011, ApJS, 195, 10

Yang G. et al., 2016, ApJ, 831, 145

APPENDIX: CATALOGUE DESCRIPTION

The description of each column of the catalogue is described in Table A1.

Table A1. 95 per cent reliability level catalogue descriptions.

Col.	Description
1	Source ID.
2	*NuSTAR* source name, following the standard IAU convention with the prefix 'NuSTAR'.
3–4	The X-ray coordinates of the source (the position of the source in which energy band has the highest DET ML).
5	The 3–24 keV band deblended DET ML (–99 if undetected).
6	The 3–24 keV band vignetting-corrected exposure time in ks at the position of the source.
7	The 3–24 keV band total counts in a 20 arcsec radius aperture.
8	The 3–24 keV band deblended background counts in a 20 arcsec radius aperture (–99 if undetected).
9	The 3–24 keV band not deblended background counts in a 20 arcsec radius aperture.
10	The 3–24 keV band net counts (deblended if detected & above DET ML threshold or 90 per cent confidence upper limit if undetected or detected but below DET ML threshold) in a 20 arcsec radius aperture.
11	The 3–24 keV band 1σ positive net counts error (–99 for upper limits).
12	The 3–24 keV band 1σ negative net counts error (–99 for upper limits).
13	The 3–24 keV band count rate (90 per cent confidence upper limit if not detected or detected but below the threshold) in a 20 arcsec radius aperture.
14	The 3–24 keV band aperture corrected flux (90 per cent confidence upper limit if not detected or detected but below threshold).
15	The 3–24 keV band positive flux error (–99 for upper limits).
16	The 3–24 keV band negative flux error (–99 for upper limits).
17–28	Source properties in 3–8 keV band with the same order as column 5–16.
29–40	Source properties in 8–24 keV band with the same order as column 5–16.
41–52	Source properties in 8–16 keV band with the same order as column 5–16.
53–64	Source properties in 16–24 keV band with the same order as column 5–16.
65	Hardness ratio computed using BEHR.
66	Upper limit of hardness ratio.
67	Lower limit of hardness ratio.
68,69	Soft X-ray (*Chandra* if having *Chandra* counterpart, otherwise XMM-*Newton*) coordinates of the associated source (–1 if no soft X-ray counterpart).
70	*NuSTAR* to soft X-ray counterpart position separation in arcsec.
71	3–8 keV flux from *XMM–Newton* (90 per cent confidence upper limit if *likemin* <6).
72	3–8 keV *XMM–Newton* flux 1σ error (−99 for upper limit).
73,74	Optical coordinates of the associated source.
75	Optical *i*-band magnitude.
76	Flag of optical *i*-band magnitude (0 = SDSS, 1 = HSC).
77,78	MMIRS coordinates of the associated source.
79,80	WISE coordinates of the associated source.
81	Spectroscopic redshift of the associated source.
82	Photometric redshift of the associated source.
83	Luminosity Distance in Mpc using the spectroscopic (if have) or photometric redshift.
84	10–40 keV band rest-frame luminosity.
85	10–40 keV band positive rest-frame luminosity error.
86	10–40 keV band negative rest-frame luminosity error.
87	Flag for sources with multiple low energy counterparts (0 = false, 1 = true).
88	Flag for sources with multiple optical and IR counterparts (0 = false, 1 = true).

This paper has been typeset from a TeX/LaTeX file prepared by the author.